

HORIZON-CL5-2022-D3-01-11

Demonstration of innovative forms of storage and their successful operation and integration into innovative energy system and grid architectures



AGISTIN

Advanced Grid Interfaces for
innovative Storage INtegration

D3.3: Methods and provision of open-source code for AGI operation

Document properties

FUNDING PROGRAM	HORIZON EUROPE
GRANT AGREEMENT NUMBER	101096197
PROJECT	AGISTIN
DELIVERABLE ID	D3.3
TITLE	<i>D3.3: METHODS AND PROVISION OF OPEN-SOURCE CODE FOR AGI OPERATION</i>
DISTRIBUTION LEVEL	PU
DUE DATE	31 DECEMBER 2025
DATE SUBMITTED	29 DECEMBER 2025
VERSION	1.0
WORK PACKAGE	WP 3
LEAD PARTICIPANT	ETH ZURICH
TOTAL NUMBER OF PAGES	58

All intellectual property rights are owned by the AGISTIN consortium members and are protected by the applicable laws. Except where otherwise specified, all document contents are: “© AGISTIN project - All rights reserved”. Reproduction is not authorised without prior written agreement. The commercial use of any information contained in this document may require a license from the owner of that information.

All AGISTIN consortium members are also committed to publish accurate and up to date information and take the greatest care to do so. However, the AGISTIN consortium members cannot accept liability for any inaccuracies or omissions, nor do they accept liability for any direct, indirect, special, consequential or other losses or damages of any kind arising out of the use of this information.

Views and opinion stated in this report reflects the opinion of the authors and not the opinion of the European Commission. The European Union is not liable for any use that may be made of the information contained in this document.

Version history

VERSION	DATE	COMMENT
0.1	17 DECEMBER 2024	STRUCTURING
0.2	05 JANUARY 2025	CONTROL PART
0.4	11 JANUARY 2025	OPTIMIZATION PART
0.7	25 OCTOBER 2025	VERSION SENT FOR REVIEW
0.9	13 DECEMBER 2025	FINAL VERSION
1.0	29 DECEMBER 2025	READY FOR SUBMISSION





EXECUTIVE SUMMARY

Grid-forming (GFM) control and dynamic ancillary services are critical for enhancing power grid stability and performance, especially with the increasing integration of AC and DC distributed energy resources (DERs). A power electronic interface with GFM capability is essential to enable DERs to collectively exhibit GFM behaviour. However, developing such an interface faces challenges, including the diversity of AC/DC conversion topologies, the distinct control needs of DERs based on their primary energy sources and power support capabilities, and the need to meet specific grid response requirements like fast frequency response (FFR). To address these challenges, the AGISTIN project has introduced the concept of advanced grid interfaces (AGIs). AGIs facilitate power conversion, coordinate heterogeneous DER dynamics, and deliver optimal performance to meet grid code demands and dynamic ancillary service incentives. This deliverable outlines a two-part solution: first, a closed-loop optimization method based on local grid perception to determine the desired dynamic performance for AGI control design; second, an aggregate GFM control strategy for AGIs to achieve this performance. This deliverable provides a comprehensive framework for coordinating diverse DERs, ensuring grid stability, and optimizing ancillary services in modern power systems.

In this deliverable, we propose a systematic closed-loop approach to provide optimal dynamic ancillary services with converter-interfaced resources based on local power grid perception. In particular, we structurally encode dynamic ancillary services such as fast frequency and voltage regulation in the form of a *parametric* transfer function matrix, which includes several parameters to define a set of different feasible response behaviours, among which we aim to find the optimal one to be realized by the converter system. Our approach is based on a so-called “*perceive-and-optimize*” (*P&O*) strategy: First, we identify a grid dynamic equivalent at the interconnection terminals of the converter system. Second, we consider the closed-loop interconnection of the identified grid equivalent and the parametric transfer function matrix, which we optimize for the set of transfer function parameters, resulting in a stable and optimal closed-loop performance for ancillary services provision. In the process, we ensure that grid-code and device-level requirements are satisfied. Finally, we demonstrate the effectiveness of our approach in different numerical case studies based on a modified Kundur two-area test system.

In this deliverable, we also present an aggregate grid-forming control for heterogeneous distributed DERs. The proposed control achieves a desired, aggregated grid-forming response by coordinating power contributions among multiple different DERs. Unlike existing aggregate control strategies that are typically objective-specific or topology-specific, we propose a generic, flexible, and modular control design. The design supports four basic module types—AC- or DC-coupling and AC- or DC-output topological arrangements—adequately accommodating diverse DER integration scenarios, e.g., AC, DC, AC/DC hybrid microgrids, hybrid energy storage systems, or hybrid renewable power plants. The grid-forming control design is systematically developed by aggregating DER dynamics and disaggregating control objectives for the four basic modules, then extended to modular configurations through a top-down approach. The grid-forming performance is comprehensively validated through simulation. This modular control design provides scalable and standardizable grid interfaces, enabling effective aggregation of heterogeneous DERs to jointly achieve grid-forming control and fast grid ancillary services.

TABLE OF CONTENTS

Introduction	1
1 Optimization and Control Framework of AGIs	6
1.1 Optimization Problem Formulation.....	6
1.1.1 Frequency-Domain Reformulation of Dynamic Ancillary Services.....	6
1.1.2 Perceive-&-Optimize (P&O) Closed-Loop Optimization.....	11
1.2 Control Problem Formulation.....	12
1.2.1 AGI Configurations.....	12
1.2.2 Aggregate Grid-Forming Control.....	13
2 Optimal Dynamic Ancillary Services Provision	16
2.1 Grid Dynamic Equivalent Identification	16
2.2 Closed-Loop Power Grid Optimization	17
3 Aggregate Grid-Forming Control Design	21
3.1 Aggregation Condition for Distributed Energy Resources.....	21
3.2 Coordinated Disaggregation of the Desired Behaviour	21
3.3 Implementable Local Control Strategies	22
3.4 Extension to Modular AC/DC Hybrid AGIs.....	23
4 Simulation Validations.....	25
4.1 Optimal Dynamic Ancillary Service Validation	25
4.1.1 Simulation Setup.....	25
4.1.2 Case Study C: Nominal Grid Conditions.....	28
4.1.3 Case Study D: Oscillatory Grid Conditions with Multiple Reserve Units	31
4.2 Aggregate Control Performance Validation	33
4.2.1 Simulation Setup.....	33
4.2.2 Case Study A: Connection to an Infinite-Bus System.....	36
4.2.3 Case Study B: Connection to the IEEE 13-Bus System.....	40
5 Conclusion	41
A. Appendix A Dynamic Ancillary Services as Transfer Functions	42
A.1 Translated Parametric Transfer Functions.....	42
A.2 Ancillary Services Constraints.....	42
B. Appendix B H2 Optimization Problem.....	45
C. Appendix C Control Objectives and Designs for Basic AGIs	46
C.1 AC-Coupled DC-Output Grid Interface.....	46
C.2 AC-Coupled AC-Output Grid Interface.....	46
C.3 DC-Coupled DC-Output Grid Interface.....	47



References 48



List of Figures

Figure 0-1 – Exemplary active power time-domain capability curve for FCR provision after a frequency step change [1]. The minimum curve requirement is shown in red (representing the lower bound of the open-loop response curve)..... 2

Figure 0-2 – Sketch of a grid-connected reserve unit to provide closed-loop optimal dynamic ancillary services in the form of a desired rational transfer function matrix $T_{d\text{ess},\alpha}^*$. The identified grid dynamic equivalent is captured by G_s 2

Figure 0-3 – Four basic grid interfaces: (A) AC-coupled AC-output configuration; (B) DC-coupled AC-output configuration; (C) AC-coupled DC-output configuration; (D) DC-coupled DC-output configuration. In either interface, all controllable DERs are aggregated to provide the desired AC or DC GFM response. 4

Figure 0-4 – A modular AC/DC hybrid grid interface, where a DC-coupled AC-output main interface, a DC-coupled DC-output sub-interface, and an AC-coupled DC-output sub-interface are included. 4

Figure 1-1 – Examples of piece-wise linear time-domain grid-code curves (simplified) and their approximation as rational parametric transfer functions..... 8

Figure 1-2 – Examples of dynamic ancillary services products (simplified) encoded as rational parametric transfer functions..... 10

Figure 1-3 – Closed-loop interconnection of the identified grid dynamic equivalent G_s with the rational parametric transfer function matrix $T_{d\text{ess},\alpha}$ which is optimized for dynamic ancillary services provision. 11

Figure 1-4 – Flowchart of the proposed “perceive-and-optimize” (P&O) approach for optimal dynamic ancillary services provision based on power grid perception..... 12

Figure 1-5 – Control objective sketch of a DC-coupled AC-output grid interface..... 14

Figure 2-1 – Grid dynamic equivalent identification setup. 16

Figure 2-2 – Closed-loop interconnection for \mathcal{H}_2 optimization. The state vector x_g results from the extended state-space representation in (2-7) of the grid dynamic equivalent, which additionally outputs the approximate integral of Δf and Δv 18

Figure 3-1 – Control design flowchart for a DC-coupled AC-output grid interface..... 22

Figure 3-2 – Control block diagram of a DC-coupled AC-output grid interface, displaying two control implementation options for the inverter: A. AC-DC matching and B. AC p-f forming, and two control implementation options for the DC-DC converters: I. DC grid-supporting and II. DC grid-forming. Note that, the aggregation of T_{is} satisfies the condition in (3-3) concerning both $T_{desvdcfs}$ and T_{desfps} and therefore, the desired behaviour for both can be achieved, even though only one (i.e., option A or B) is implemented explicitly in the inverter, as the other one is achieved implicitly. 23

Figure 4-1 – One-line diagram of the three-phase two-area test system with two converter-based reserve units for optimal dynamic ancillary services provision. 25

Figure 4-2 – One-line diagram of three-phase power converter interface of one reserve unit including grid equivalent identification and matching control..... 27

Figure 4-3 – Active and reactive power response after a negative frequency and voltage step change for the cheap $T_{d\text{ess},\alpha 0}$ which satisfies minimal grid-code requirements (cf. grid-code examples in Figure 1-1 and Figure 1-2). 27

Figure 4-4 – Grid dynamic equivalent identification of the two-area system..... 28

Figure 4-5 – Bode diagrams of the identified 2×2 grid dynamic equivalent G_{1s} for the nominal two-area system in Figure 4-4(a)..... 29



Figure 4-6 – Open-loop active and reactive power step responses after a negative frequency and voltage step change for the optimal $T_{des, 1s, \alpha_{nom}}$ and the cheap $T_{des, 1s, \alpha_0}$, respectively.29

Figure 4-7 – Closed-loop system response behaviour of the nominal two-area system after a load increase at bus 7 for the optimal $T_{des, 1s, \alpha_{nom}}$ and the cheap $T_{des, 1s, \alpha_0}$, respectively.....30

Figure 4-8 – Closed-loop response behaviour of the two-area system following a load increase at bus 7, analysed for the optimal $T_{des, 1s, \alpha_{nom}}$ in a nominal scenario (fat curve) and in Monte Carlo simulations with randomly varied active power generation set points of the SGs within a $\pm 10\%$ range (thin curves).....30

Figure 4-9 – Bode diagrams of the identified 2×2 grid dynamic equivalent G_1s for the oscillatory two-area system in Figure 4-4(a) during the first P&O cycle.31

Figure 4-10 – Open-loop active and reactive power step responses after a negative frequency and voltage step change for the optimal $T_{des, 1s, \alpha_{osci}}$ and the cheap $T_{des, 1s, \alpha_0}$, respectively.....31

Figure 4-11 – Closed-loop system response behaviour of the oscillatory two-area system after a load increase at bus 7. We compare the optimal $T_{des, 1s, \alpha_{osci}}$, the nominal $T_{des, 1s, \alpha_{nom}}$, and the cheap $T_{des, 1s, \alpha_0}$, of reserve unit 1, respectively. Reserve unit 2 is always realizing the cheap $T_{des, 2s, \alpha_0}$32

Figure 4-12 – Closed-loop system response behaviour of the oscillatory two-area system after a load increase at bus 7. We compare the initial system configuration based on the cheap $T_{des, 1s, \alpha_0}$ and $T_{des, 2s, \alpha_0}$ of both units, with the optimal $T_{des, 1s, \alpha_{osci}}$ of unit 1 after the first P&O cycle and the optimal $T_{des, 2s, \alpha_{osci}}$ of unit 2 after the second P&O cycle.....33

Figure 4-13 – Illustration of the system setup in case studies. (a) A basic DC-coupled AC-output grid interface. (b) A multi-DC-bus interface. (c) An AC/DC hybrid interface. (d) A DC-coupled AC-output grid interface connected to the IEEE 13-bus system.....34

Figure 4-14 – Magnitude Bode plots, where $T_{desvdcf} - 1T_{desfp} - 1$ denotes the desired power response; T_{sc} , T_{bess} , and T_{pv} the power responses of the DERs; T_{desfp} the desired frequency response; and $T_{desvdcf} - 1iTi - 1$ the desired frequency response using causalized T_i or $T_i - 1$. (a) For the DC grid-supporting implementation. (b) For the DC grid-forming implementation.....36

Figure 4-15 – Simulation results of case study A1: the basic grid interface in Figure 4-13(a) under a grid frequency dip and a voltage dip. The control of the DC-DC converters uses (a) DC grid-supporting implementation and (b) DC grid-forming implementation. The ripples in the waveforms are due to the IGBT switching.....36

Figure 4-16 – Simulation results of case study A2: the basic grid interface in Figure 4-13(a) with different coordination between the DERs. (a) Different inertia time constants τ_{sc} in the SC's power response $T_{sc} = -\tau_{sc}s0.01s + 1$. (b) Different participation factor static gains η_{pv} in the PV's power response $T_{pv} = \eta_{pv}0.5s + 1T_{bess\&pv}$37

Figure 4-17 – Simulation results of case study A3: the multi-DC-bus grid interface in Figure 4-13(b) under a grid frequency dip.....38

Figure 4-18 – Simulation results of case study A4: the AC/DC hybrid grid interface in Figure 4-13(c) under a grid frequency dip.....38

Figure 4-19 – Simulation results of case study B1: the grid interface connected to the IEEE 13-bus system in Figure 4-13(d) under load change and recovery.....39

Figure 4-20 – Simulation results of case study B2: the grid interface connected to the IEEE 13-bus system in Figure 4-13(d) under a grid short-circuit fault.....39



LIST OF TABLES

Table 1-1 – Grid-code and device-level specification examples.....	8
Table 1-2 – Control objectives and control designs of the four basic grid interfaces.....	15
Table 4-1 – Main parameters of the SGs in the nominal two-area system.....	26
Table 4-2 – Converter parameters of reserve units 1 and 2.	26
Table 4-3 – Optimal transfer function parameters $\alpha *$ for case studies C and D.	32
Table 4-4 – Parameters in simulation validations of AGI dynamic performance.	34

Abbreviations and Acronyms

AC	Alternating Current
AGI	Advanced Grid Interface
ARX	AutoRegressive with eXogeneous input
AVR	Automatic Voltage Regulator
BESS	Battery Energy Storage System
DC	Direct Current
DER	Distributed Energy Resource
DVPP	Dynamic Virtual Power Plant
FCR	Frequency Containment Reserve
FFR	Fast Frequency Response
GFM	Grid Forming
HVDC	High Voltage Direct Current
IGBT	Insulated Gate Bipolar Transistor
LPV	Linear Parameter Varying
PCC	Point of Common Coupling
PEM	Prediction Error Method
PI	Proportional Integral
P&O	Perceive & Optimize
POD	Power Oscillation Damping
PSS	Power System Stabilizer
PWM	Pulse Width Modulation
RoCoF	Rate of Change of Frequency
SC	Supercapacitor
SG	Synchronous Generator
STATCOM	Static Synchronous Compensator
VPP	Virtual Power Plant



Introduction

Grid-forming (GFM) control and dynamic ancillary services have gained wide recognition in recent years for enhancing the stability and dynamic performance of power grids, particularly with the growing penetration of distributed energy resources (DERs). A power electronic interface capable of GFM functionality is essential for enabling DERs to exhibit GFM behaviours when connected to the grid. Given the small capacity of individual DERs, *such a grid interface must be capable* of coordinating heterogeneous DERs to provide a collective GFM response. However, developing this GFM interface presents several challenges. First, DERs may be interconnected with the grid through various AC/DC power conversion topologies. Second, due to the diverse nature of primary energy sources, each DER typically requires distinct control behaviours depending on their power and energy capabilities over different time scales, while their collective behaviours must also be effectively coordinated. Third, a desired GFM interface should meet specific response requirements like fast frequency response (FFR), as demanded by grid codes or incentives for optimal dynamic ancillary services beyond grid code requirements. To address these challenges, the concept of advanced grid interfaces (AGIs) was introduced by the EU's Horizon project AGISTIN. The AGI is crucial to control power conversion between DERs and the power grid, coordinate the dynamic response of heterogeneous DERs, and achieve the desired or optimal dynamic performance.

The first part of this deliverable presents a closed-loop optimization approach to provide optimal dynamic ancillary services based on local power grid perception. The approach outputs the desired dynamic performance for the control design of AGIs. The second part of this deliverable presents an aggregate GFM control of the AGI to achieve the desired dynamic performance.

The grid-code compliance and further optimal dynamic ancillary services of grid interfaces are of importance to ensure grid dynamic performance. Currently, grid-code specifications for dynamic ancillary services provision (e.g., fast frequency and voltage regulation) with converter-interface generation are typically defined by a prescribed time-domain step-response characteristic [1][2][3][4]. As an example, the European network code [1], which is adopted in most European national grid codes, specifies the active power provision for frequency containment reserve (FCR) in response to a frequency step change by a piece-wise linear time-domain curve (Figure 0-1). Likewise, the dynamic response of reactive power for voltage regulation is defined via time-domain specifications in response to a voltage step change [1]. Recent grid codes (e.g., Finland [2], Ireland [3], Sweden/Norway/Denmark [4]) also define the activation of fast frequency reserves (FFR) or synthetic inertia response via piece-wise linear active power curves in the time domain. Such grid codes aim to integrate power converters into low-inertia grids and are important measures to ensure the transition toward converter-dominated power systems.

Although the specification of the piece-wise linear time-domain curves in today's grid codes is straightforward, they only assign the lower bound of the open-loop response characteristic for an ancillary services-providing reserve unit (see, e.g., the red curve in Figure 0-1). On the one hand, different dynamic responses of a reserve unit are allowed, as long as the grid-code requirements are satisfied at or above the piece-wise linear curves. This results in a family of different feasible response behaviours, where the reserve unit injection is often pared down to the minimum by just satisfying the grid-code requirements at its boundaries. On the other hand, the current grid-code specifications are indistinguishable for any location of converter-interfaced generation, regardless

of the grid strength and dynamic characteristics at the grid-connection point. However, in future power systems with increased penetration of converter-interfaced generation, such indistinguishable grid-code specifications in an open-loop manner will result in a sub-optimal closed-loop power system response with poor dynamic performance or even unstable behaviours [5][6]. In this regard, existing studies in [7][8][9] have indicated that the location of synthetic inertia and damping should be carefully chosen to provide better stability and dynamic performance. Therefore, future grid-code specifications for dynamic ancillary services provision may have to respect distinguishably the local grid dynamic characteristics in a closed-loop manner.

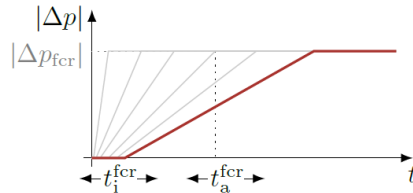


Figure 0-1 – Exemplary active power time-domain capability curve for FCR provision after a frequency step change [1]. The minimum curve requirement is shown in red (representing the lower bound of the open-loop response curve).

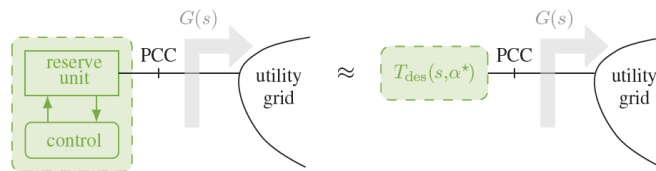


Figure 0-2 – Sketch of a grid-connected reserve unit to provide closed-loop optimal dynamic ancillary services in the form of a desired rational transfer function matrix $T_{des}(s, \alpha^*)$. The identified grid dynamic equivalent is captured by $G(s)$.

Moreover, beyond the flaw of specifying an open-loop response characteristic and being indistinguishable for any power grid condition, the practical implementation of the piece-wise linear time-domain grid-code curves in converters is not immediate, and no systematic methods have been developed yet. In this regard, today’s industrial practice is often ad-hoc and highly customized, e.g., relying on open-loop trajectory commands [10], varying gains [11], or look-up table schemes [12] to approximately satisfy the grid codes. The design, implementation, and tuning of such methods, however, are in general time-consuming and rigid, which impedes its applicability.

To overcome the previous shortcomings, this deliverable proposes a closed-loop approach to provide optimal dynamic ancillary services with AGIs, based on local power grid perception, which systematically ensures that open-loop grid code requirements and device-level limitations are reliably satisfied. Specifically, we translate the aforementioned time-domain grid-code capability curves into a rational parametric transfer function matrix $T_{des}(s, \alpha)$ in the frequency domain, which defines a tractable desired response behaviour to be realized by the converter (see Figure 0-2). The parameter vector α establishes a set of feasible response behaviours constrained by the grid-code and device-level limitations, out of which we aim to find the optimal behaviour such that a stable and optimal closed-loop performance of the entire power system can be achieved. As the main contribution for the optimization of AGIs, we introduce a so-called “perceive-and-optimize” (P&O) strategy, which is composed of two main steps: We first use the grid-connected converter to identify a grid dynamic equivalent $G(s)$ at its interconnection terminals (“perceive”). Second, we consider the closed-loop interconnection of the identified grid dynamic equivalent $G(s)$ and the AGI

(represented by the parametric transfer function matrix $T_{\text{des}}(s, \alpha)$), where we optimize α to achieve an optimal and stable closed-loop performance of the entire power grid response, while ensuring grid-code and device-level requirements to be reliably satisfied (“optimize”).

Numerous studies have explored the optimization of dynamic ancillary services provision, as evidenced by [7][8]. These endeavours rely on an offline design using precise knowledge of the dynamic power system model or its approximation, which, however, is typically unavailable in practice. Moreover, these methods failed to consider potential variations in grid conditions over time. Conversely, alternative approaches, exemplified by [13], proposed adaptive tuning methods to enhance the dynamic response behaviour of grid-connected converter systems based on local power grid measurements, thereby taking a similar P&O perspective as proposed in our work. Despite its innovation, however, the suggested concept in [13] is highly specialized and confined to providing power oscillation damping services, lacking immediate adaptability to other dynamic ancillary service products. Notably, none of the methods outlined in [7][8][13] account for grid-code or device-level requirements. This stands in vast contrast to our method for optimal dynamic ancillary services, characterized by its ability to:

- perceive local grid dynamics,
- attain optimal performance in a closed loop with the grid,
- encode grid-code and device-level requirements,
- accommodate time-varying grid conditions, and
- offer a systematic and versatile approach applicable to a wide range of dynamic ancillary services products.

The desired dynamic performance of AGIs, determined by the optimization approach, dictates the subsequent control design. This control design aims to achieve the specified dynamic response by coordinating multiple DERs through the grid interface. Several basic grid interfaces are shown in Figure 0-3. Precisely, grid interfaces can collectively integrate, coordinate, and aggregate DERs (involving generation, storage, loads, etc.) to provide a desired GFM response to the grid. The interface configurations depicted in Figure 0-3 and Figure 0-4 include various AC and DC coupling types and output types, effectively capturing the diverse topological arrangements for integrating DERs into power grids [14][15][16], such as AC, DC, AC/DC hybrid microgrids, hybrid renewable power plants, aggregation of DERs. While the GFM control of individual DERs has been extensively studied [17], the aggregate GFM control of multiple heterogeneous DERs, particularly in AC/DC hybrid configurations, remains a relatively underexplored area. Existing control strategies can be broadly classified into two categories, based on the perspectives of microgrids and virtual power plants (VPPs), respectively.

In the area of microgrids, droop control has been widely used. In AC microgrids, droop control encodes the static power coordination of DERs, whose aggregate response [18] may not ensure the desired response demand on the AC-coupling bus [19]. A DC microgrid can also be enabled to provide AC GFM behaviours when connected to an AC grid and using GFM controls in the grid-connected inverter, e.g., droop control [20][21], virtual synchronous machine [22][23], matching control [24], or dual-port power-balancing control [25]. The DERs in such DC microgrids should be coordinated dynamically to stabilize the DC-bus voltage. For instance, a proportional-integral (PI) controller cascaded with a low-pass filter and a high-pass filter is applied to battery energy storage systems (BESSs) and supercapacitors (SCs), respectively, in [24][26]. Similarly, a PI controller is

applied to BESSs while a purely proportional controller is used for SCs in [27]. These coordination strategies for distinct types of DERs are specifically designed to stabilize the DC-bus voltage while not necessarily providing a desired dynamic response behaviour on the DC-coupling bus. Since the primary objective in both AC and DC microgrids is autonomous power and energy management, there are no explicit requirements and mechanisms for dynamic aggregation of DERs. This suggests that existing microgrid control strategies are inadequate for GFM control of DER aggregation.

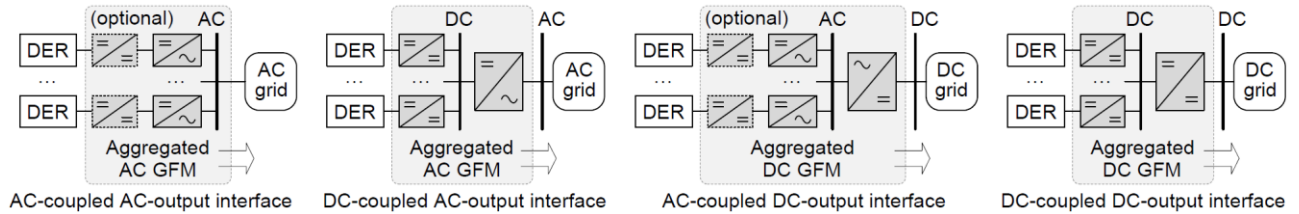


Figure 0-3 – Four basic grid interfaces: (A) AC-coupled AC-output configuration; (B) DC-coupled AC-output configuration; (C) AC-coupled DC-output configuration; (D) DC-coupled DC-output configuration. In either interface, all controllable DERs are aggregated to provide the desired AC or DC GFM response.

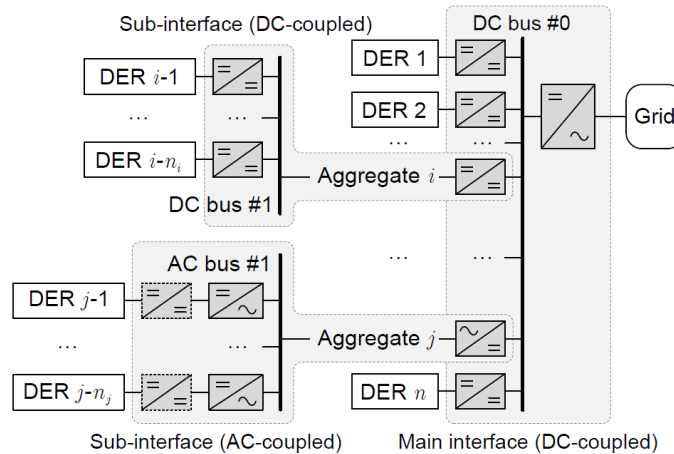


Figure 0-4 – A modular AC/DC hybrid grid interface, where a DC-coupled AC-output main interface, a DC-coupled DC-output sub-interface, and an AC-coupled DC-output sub-interface are included.

Another category of control strategies more relevant to aggregate grid interfaces appears from the topic of virtual power plants (VPPs). Conceptually, VPPs are a collection of DERs aggregated to improve energy management and trading [28][29]. Most commercial VPPs provide ancillary services, ranging from primary and secondary regulation to dispatch and electricity markets [30][31]. However, the current VPPs do not usually address faster time scales of dynamic response, e.g., FFR. The concept and strategies of dynamic VPPs (DVPPs) have been advocated in recent years to enable fast dynamic ancillary services of DER aggregation [19][32][33]. Notably, a flexible control design for a GFM DVPP grid interface is explored in [19]. However, this control design is limited to an AC-coupled configuration and the output terminal can only be connected to an AC grid, i.e., topology-specific. For this reason, there is a lack of more generic grid interface designs that address AC, DC, and AC/DC hybrid arrangements for DER aggregation.

Overall, despite considerable research on the coordinated or aggregate control of DERs in the areas of microgrids and DVPPs, existing control designs struggle to meet the flexible control objectives required by grid codes and enabled by advanced GFM interfaces. In particular, existing controls are typically objective-specific and may lack the flexibility to deliver a desired aggregate response



(typically required by grid codes [34] or ancillary service markets [35]) to the AC or DC coupling bus and the grid. Additionally, existing control designs are typically topology-specific, while not easily scalable to accommodate generic AC/DC hybrid systems.

Therefore, the control part of this deliverable explores a wide range of grid interfaces including AC-coupled, DC-coupled, AC-output, and DC-output configurations, i.e., presenting four basic grid interfaces. These basic modules can be interconnected to form a modular AC/DC hybrid grid interface. The modular interface design offers high flexibility in achieving a desired dynamic response, high scalability in modular configuration and control, uniform standardization for multi-AC/DC-port interconnections, and high transparency of dynamic behaviours. The major contributions of the control method are summarized as follows.

- We formulate desired and interoperable control objectives for the four basic grid interface configurations/modules that represent four typical topological arrangements in the current DER integration practice.
- We propose a GFM control design for each basic interface, including the condition for DER aggregation, the coordinated disaggregation of the desired behaviour, and the local control strategies for individual converters.
- We extend the control designs to include modular AC/DC hybrid grid interfaces using a systematic top-down design approach, offering a highly flexible and scalable solution for GFM control of DER aggregation.

The deliverable is structured as follows. Chapter 1 introduces various AGI configurations and an upper-layer optimization and bottom-layer control framework. In Chapter 2, we present the novel P&O strategy for optimal dynamic ancillary services provision. The aggregate GFM control design is detailed in Chapter 3. Simulation validations are presented in Chapter 4. Finally, Chapter 5 concludes this deliverable.

1 Optimization and Control Framework of AGIs

The optimization of AGIs is to provide a desired optimal dynamic ancillary service provision based on the local grid characteristics. The control of AGIs is aimed to achieve the desired dynamic response behaviour by coordinating and aggregating multiple AC and DC DERs. This chapter presents an optimization and control framework for AGIs, including the formulation of control and optimization problems.

1.1 Optimization Problem Formulation

1.1.1 Frequency-Domain Reformulation of Dynamic Ancillary Services

We consider dynamic ancillary services to be encoded in the form of a rational parametric transfer function matrix $T_{\text{des}}(s, \alpha)$ in the frequency domain (with parameter vector $\alpha = [\alpha^{\text{fp}}, \alpha^{\text{vq}}]$), specifying a desired decoupled frequency and voltage control behaviour to be realized by a reserve unit, i.e.,

$$\begin{bmatrix} \Delta p(s) \\ \Delta q(s) \end{bmatrix} = \underbrace{\begin{bmatrix} T_{\text{des}}^{\text{fp}}(s, \alpha^{\text{fp}}) & 0 \\ 0 & T_{\text{des}}^{\text{vq}}(s, \alpha^{\text{vq}}) \end{bmatrix}}_{=T_{\text{des}}(s, \alpha)} \begin{bmatrix} \Delta f(s) \\ \Delta v(s) \end{bmatrix}, \quad (1-1)$$

where Δf and Δv are the measured bus frequency and voltage magnitude deviation, and Δp and Δq the active and reactive power output deviations (deviating from the respective power set point). In particular, the transfer function matrix in (1-1) defines a tractable response behaviour which can be easily realized in standard converter control architectures as a reference model to be matched. Following current grid-code specifications for transmission networks, we stick to a classical decoupled grid-following frequency and voltage regulation in (1-1). However, our formalism directly extends to fully coupled multi-input multi-output specifications for $T_{\text{des}}(s, \alpha)$, potentially relevant for future ancillary services or in other types of networks [36]. Moreover, also grid-forming implementations with inverse signal causality can be considered [19].

The transfer functions in (1-1) are defined as a superposition of different dynamic ancillary services products $T_{\text{des}}^{\text{fp},i}(s, \alpha^{\text{fp},i})$ and $T_{\text{des}}^{\text{vq},i}(s, \alpha^{\text{vq},i})$ (acting on different time-scales [37]), i.e.,

$$\begin{aligned} T_{\text{des}}^{\text{fp}}(s, \alpha^{\text{fp}}) &= \sum_i T_{\text{des}}^{\text{fp},i}(s, \alpha^{\text{fp},i}), \\ T_{\text{des}}^{\text{vq}}(s, \alpha^{\text{vq}}) &= \sum_i T_{\text{des}}^{\text{vq},i}(s, \alpha^{\text{vq},i}). \end{aligned} \quad (1-2)$$

where the parametric structure of $T_{\text{des}}^{\text{fp},i}(s, \alpha^{\text{fp},i})$ and $T_{\text{des}}^{\text{vq},i}(s, \alpha^{\text{vq},i})$ results from the different grid-code requirements of each dynamic ancillary services product i , as detailed below.

- Frequency Regulation

Nowadays, typical dynamic ancillary service products for frequency regulation are frequency containment reserve (FCR) [1], fast frequency response (FFR) [2][3][4], and other auxiliary controls such as power oscillation damping (POD) [1][38]. We can specify $T_{\text{des}}^{\text{fp}}(s, \alpha^{\text{fp}})$ in (1-2) as

$$T_{\text{des}}^{\text{fp}}(s, \alpha^{\text{fp}}) = T_{\text{des}}^{\text{fcr}}(s, \alpha^{\text{fcr}}) + T_{\text{des}}^{\text{ffr}}(s, \alpha^{\text{ffr}}) + T_{\text{des}}^{\text{aux}}(s, \alpha^{\text{aux}}), \quad (1-3)$$

where $T_{des}^{fcr}(s, \alpha^{fcr})$ encodes the FCR provision, $T_{des}^{ffr}(s, \alpha^{ffr})$ the FFR provision, and $T_{des}^{aux}(s, \alpha^{aux})$ defines an auxiliary service to damp high-frequency dynamics and/or power oscillations. Of course, depending on the requirements of different grid codes and reserve units, one might also consider other types of dynamic ancillary services products. Moreover, notice that different grid codes or market formats might support either a simultaneous provision of several ancillary services products by one reserve unit (see, e.g., Section 5 in the Finish grid code [2]), or a separate provision of services by different units. In any case, we propose a generic approach which is compatible with either option, i.e., capable of considering one, two, or multiple types of ancillary services products in (1-3). For the sake of simplicity (and without loss of generality), we stick to the superposition of the three products in (1-3) in the following.

The structure and parameters of the transfer function terms in (1-3) can be obtained from the underlying grid-code specification of each ancillary service product. For instance, in the case of the FCR and FFR provision, the associated grid-code specifications are typically defined by some prescribed piece-wise linear time-domain curves (Figure 1-1), where the required active power response should be satisfied at or above some minimum requirements. By applying our recent method in [34] (which is based on Laplace transformations followed by Padé approximations of appropriate order), we can translate such piece-wise linear time-domain curves into the aforementioned rational parametric transfer functions $T_{des}^{fcr}(s, \alpha^{fcr})$ and $T_{des}^{ffr}(s, \alpha^{ffr})$ in the frequency domain, respectively (the explicit expressions are stated in (A-1) in Appendix A. The parameter vector α used in these transfer functions contains the parameters of the time-domain curves, which have to satisfy certain grid-code and device-level requirements.

As an example, for the parameters $\alpha^{fcr} := [t_i^{fcr}, t_a^{fcr}]$ of the FCR curve in Figure 1-1(a), we require [1]

$$\begin{aligned} 0 &\leq t_i^{fcr} \leq t_{i,max}^{fcr} \\ t_i^{fcr} &\leq t_a^{fcr} \leq t_{a,max}^{fcr} \\ |\Delta p_{fcr}^{max}| &\leq (t_a^{fcr} - t_i^{fcr}) \cdot r_{max}^p, \end{aligned} \quad (1-4)$$

where $t_{i,max}^{fcr}$ and $t_{a,max}^{fcr}$ are the maximum admissible FCR initial delay and activation times, $|\Delta p_{fcr}^{max}| = |1/D_p \Delta f_{max}|$ is the maximum FCR capacity, and r_{max}^p is the maximal active power ramping rate of the reserve unit, as specified in Table 1-1 and graphically illustrated by the minimum curve requirement (red) in Figure 1-1(a). Hence, as indicated by the family of light grey curves in Figure 1-1(a), the requirements in (1-4) establish a set of different feasible response behaviours for the reserve unit. For a particular feasible α^{fcr} as for the bold gray curve in Figure 1-1(a), the unit step response of the associated translated transfer function $T_{des}^{fcr}(s, \alpha^{fcr})$ is exemplarily indicated by the black dashed line. Finally, the requirements (1-4) can be divided into grid-code and device-level specifications as

$$\alpha^{fcr} \in \mathcal{G}^{fcr} \cap \mathcal{D}^{fcr}, \quad (1-5)$$

where the grid-code specification set \mathcal{G}^{fcr} is defined by the constraints in the first two sub-questions in (1-4), and the device-level limitation set \mathcal{D}^{fcr} by the constraint in the last sub-equation in (1-4), respectively.

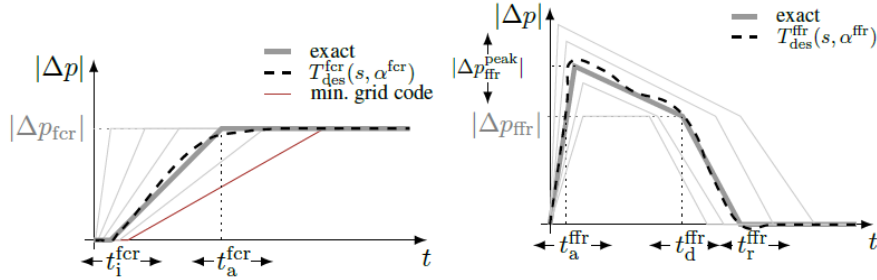
Table 1-1 – Grid-code and device-level specification examples.

(a) Grid-code specifications (exemplary values adopted from [1]–[3], [38]).

Parameter	Symbol	Value
Maximum admissible initial delay time for FCR	$t_{i,\max}^{\text{fcr}}$	2 s
Maximum admissible full activation time for FCR	$t_{a,\max}^{\text{fcr}}$	30 s
Maximum admissible full activation time for FFR	$t_{a,\max}^{\text{ffr}}$	2 s
Minimum support duration time for FFR	$t_{d,\min}^{\text{ffr}}$	$8 \text{ s} + t_a^{\text{ffr}}$
Minimum return-to-recovery time for FFR	$t_{r,\min}^{\text{ffr}}$	$10 \text{ s} + t_d^{\text{ffr}}$
Maximum overdelivery factor during FFR	x_{\max}^{ffr}	1.35
Minimum frequency for oscillation damping	ω_{\min}	$2\pi \cdot 0.1 \text{ rad/s}$
Maximum frequency for oscillation damping	ω_{\max}	$2\pi \cdot 3 \text{ rad/s}$
Maximum admissible 90% reactive power activation time	$t_{90,\max}^{\text{vq}}$	5 s
Maximum admissible 100% reactive power activation time	$t_{100,\max}^{\text{vq}}$	60 s

(b) Device-level specifications (values depend on the reserve unit).

Parameter	Symbol
Maximum active power ramping rate of reserve unit	$r_{\max}^p = R_{\max}^p \cdot \Delta f_{\max}$
Maximum reactive power ramping rate of reserve unit	$r_{\max}^q = R_{\max}^q \cdot \Delta v_{\max}$
Maximum active power peak capacity of reserve unit	$m_{\max}^p = M_{\max}^p \cdot \Delta f_{\max}$
Maximum FFR support duration time of reserve unit	$t_{d,\max}^{\text{ffr}}$
Maximum FFR return-to-recovery time of reserve unit	$t_{r,\max}^{\text{ffr}}$



(a) Exemplary active power time-domain capability curve for FCR provision after a frequency step change [1] (cf. Fig. 1): the reserve unit has to deliver a certain FCR capacity $|\Delta p_{\text{fcr}}|$ in accordance with an initial delay time t_i^{fcr} and a full activation time t_a^{fcr} , where the FCR capacity $|\Delta p_{\text{fcr}}|$ is typically fixed by the allocated active power droop gain D_p and the amplitude of the frequency step input Δf , i.e., $|\Delta p_{\text{fcr}}| = |\frac{1}{D_p} \Delta f|$. The minimum grid-code curve requirements are exemplarily indicated in red.

(b) Exemplary active power time-domain capability curve for FFR provision after a frequency step change [2]: the reserve unit has to deliver the FFR capacity $|\Delta p_{\text{ffr}}|$ after an activation time t_a^{ffr} , which has to remain activated until a particular support duration time t_d^{ffr} , before returning to recovery at time t_r^{ffr} . The overdelivery $|\Delta p_{\text{ffr}}^{\text{peak}}|$ is a multiple of the FFR capacity, i.e., $|\Delta p_{\text{ffr}}^{\text{peak}}| = x^{\text{ffr}} |\Delta p_{\text{ffr}}|$, where $|\Delta p_{\text{ffr}}|$ is defined by the scaled amplitude of the frequency step input, i.e., $|\Delta p_{\text{ffr}}| = |\frac{1}{K_p} \Delta f|$.

Figure 1-1 – Examples of piece-wise linear time-domain grid-code curves (simplified) and their approximation as rational parametric transfer functions.

Likewise, also the parameters $\alpha^{\text{ffr}} := [t_a^{\text{ffr}}, t_d^{\text{ffr}}, t_r^{\text{ffr}}, x^{\text{ffr}}]$ of the FFR curve in Figure 1-1(b) are subject to grid-code and device-level constraints similar to (1-4), i.e.,

$$\alpha^{\text{ffr}} \in \mathcal{G}^{\text{ffr}} \cap \mathcal{D}^{\text{ffr}}, \quad (1-6)$$

where the grid-code and device-level constraint sets \mathcal{G}^{ffr} and \mathcal{D}^{ffr} encode several time and capacity bounds as listed in Table 1-1, which establish a feasible set of response behaviours as illustrated by the family of light grey curves in Figure 1-1(b). A detailed formulation of (1-6) similar to (1-4) can be found in the grid-code documents [2][3][4] or more compactly in (A-2) in Appendix A.

In contrast to the FCR and FFR grid-code specifications, the damping of high-frequency dynamics and/or power oscillations is usually stated less specifically in today's grid codes, despite its importance for grid-connected converters to provide damping services, similar to the power system stabilizer (PSS) in synchronous generators [1]. Note that grid codes often only specify a certain range of frequencies $[\omega_{\min}, \omega_{\max}]$ in which the POD service has to be provided (e.g., Spain [38]), without prescribing a particular response behaviour for the reserve unit. In this regard, we define the parametric structure of $T_{\text{des}}^{\text{aux}}(s, \alpha^{\text{aux}})$ in the form of a bandpass resonator transfer function as in Figure 1-2(a), i.e.,

$$T_{\text{des}}^{\text{aux}}(s, \alpha^{\text{aux}}) = m_{\text{aux}} \cdot \frac{(\omega_h - \omega_l)s}{s^2 + (\omega_h - \omega_l)s + \omega_l\omega_h}, \quad (1-7)$$

which is parametric in $\alpha^{\text{aux}} = [\omega_l, \omega_h, m_{\text{aux}}]$. The auxiliary term $T_{\text{des}}^{\text{aux}}(s, \alpha^{\text{aux}})$ provides additional flexibility for optimal dynamic ancillary services provision by introducing a lead-lag compensation in the frequency domain for stability enhancements and power oscillation damping (similar to PSS in synchronous generators) to supplement the (usually slower) FCR and FFR injections as indicated in (1-3). While more general or higher-order formulations of a bandpass transfer function could be employed, we deliberately select the form in (1-7) for its pragmatic structure, allowing for physical interpretation in terms of resonance frequency and filter bandwidth, thereby facilitating the formulation of parameter constraints on α^{aux} . Namely, $\alpha^{\text{aux}} = [\omega_l, \omega_h, m_{\text{aux}}]$ has to satisfy grid-code and device-level constraints as

$$\alpha^{\text{aux}} \in \mathcal{G}^{\text{aux}} \cap \mathcal{D}^{\text{aux}}. \quad (1-8)$$

In particular, the grid-code specification set \mathcal{G}^{aux} is defined by the frequency range $[\omega_{\min}, \omega_{\max}]$ to damp high-frequency dynamics and/or power oscillations, and the device-level limitation set \mathcal{D}^{aux} limits the resonance amplitude according to the reserve unit's maximum capacity (see Table 1-1), thereby establishing a feasible set of different resonator transfer functions as indicated by the light grey curves in Figure 1-2(a). A detailed formulation of (1-8) can be found in (A-3) in Appendix A.

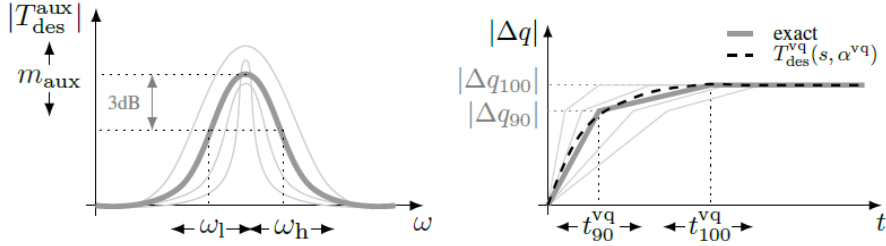
Finally, by superimposing the previous transfer functions, we can establish the overall frequency control specification $T_{\text{des}}^{\text{fp}}(s, \alpha^{\text{fp}})$ as in (1-3). In doing so, we further need to ensure that the maximum capacity and bandwidth limitations of the reserve unit are not violated during a *superimposed* injection of active power. We encode these overarching constraints via an additional overall device-level constraint set \mathcal{D}^{fp} for f-p control, which is specified in detail in (A-5) in Appendix A.

- Voltage Regulation

In analogy to the frequency regulation, we in general also consider $T_{\text{des}}^{\text{vq}}(s, \alpha^{\text{vq}})$ in (1-2) as a superposition of different voltage regulation products. The most common and often even

only specified voltage control service in today's grid codes is the dynamic activation of reactive

power proportionately to a voltage step change under particular time specifications [1]. An example of the associated piece-wise linear grid-code curve is shown in Figure 1-2(b), and the associated translated transfer function response (see (A-1) in Appendix A for a detailed expression) is indicated via black dashed lines. Notice that the voltage control provision in Figure 1-2(b) might be specified differently in different grid codes. Moreover, in the same vein as for frequency regulation, one might also further populate the voltage regulation transfer function $T_{des}^{vq}(s, \alpha^{vq})$ with some additional auxiliary term(s) for oscillation damping, etc.



(a) Exemplary magnitude Bode plot of bandpass resonator transfer function to damp high-frequency dynamics and/or power oscillations: $\omega_r = \sqrt{\omega_l \omega_h}$ is the resonance frequency, $\Delta\omega_{BW} = \omega_h - \omega_l$ the filter bandwidth, and m_{aux} the magnitude. (b) Exemplary reactive power time-domain capability curve for voltage control after a voltage step change: the reserve unit has to deliver the reactive power capacity levels $|\Delta q_{90}|$ of 90% and $|\Delta q_{100}|$ of 100% in accordance with the times t_{90}^{vq} and t_{100}^{vq} , respectively, where the reactive power capacity levels $|\Delta q_{90}|$ and $|\Delta q_{100}|$ are typically fixed by the allocated reactive power droop gain D_q and the amplitude of the voltage step input Δv , i.e., $|\Delta q_{100}| = \frac{1}{D_q} \Delta v$.

Figure 1-2 – Examples of dynamic ancillary services products (simplified) encoded as rational parametric transfer functions.

The time-parameters $\alpha^{vq} := [t_{90}^{vq}, t_{100}^{vq}]$ for the reactive power curve example in Figure 1-2(b) have to satisfy grid-code and device level requirements similar to (1-4) as

$$\alpha^{vq} \in \mathcal{G}^{vq} \cap \mathcal{D}^{vq}, \quad (1-9)$$

where the grid-code and device-level constraint sets \mathcal{G}^{vq} and \mathcal{D}^{vq} encode several time constraints as listed in Table 1-1. A detailed formulation of (1-9) similar to (1-4) can be found in the grid-code document [1] and in (A-6) in Appendix A.

Ultimately, by putting all ancillary service products together, we can establish the desired parametric transfer function matrix $T_{des}(s, \alpha)$ with parameter vector $\alpha = [\alpha^{fp}, \alpha^{vq}] \in \mathbb{R}^n$ in (1-1), where $\alpha^{fp} := [\alpha^{fcr}, \alpha^{ffr}, \alpha^{aux}]$, to encode a set of feasible response behaviours for dynamic ancillary services provision. Out of the latter, we aim to find the optimal behaviour $T_{des}(s, \alpha^*)$ as elaborated in the next section. It should be emphasized that our goal is to do more than cheaply satisfy the minimum open-loop grid-code requirements (e.g., by choosing α as the critical point where all grid-code constraints are active), with the ultimate goal being an optimal closed-loop performance regardless of the characteristics of the power grid.

1.1.2 Perceive-&Optimize (P&O) Closed-Loop Optimization

We abstract the circuit topology in Figure 0-2 and consider now a small-signal block diagram for the closed-loop interconnection of the grid dynamic equivalent $G(s)$ and the rational parametric transfer function matrix $T_{\text{des}}(s, \alpha)$ for dynamic ancillary services provision as depicted in Figure 1-3.

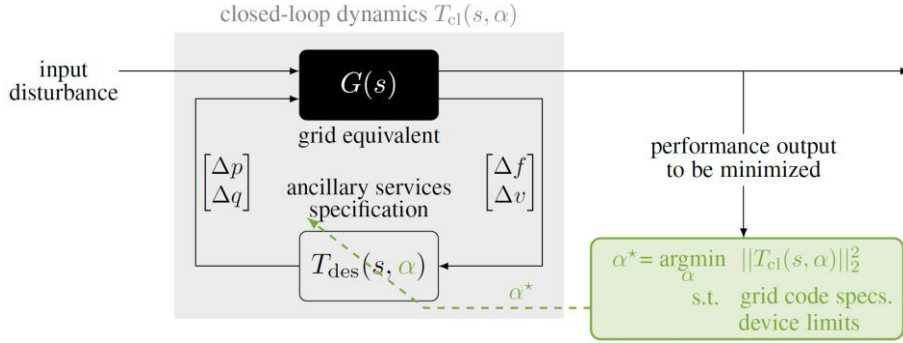


Figure 1-3 – Closed-loop interconnection of the identified grid dynamic equivalent $G(s)$ with the rational parametric transfer function matrix $T_{\text{des}}(s, \alpha)$ which is optimized for dynamic ancillary services provision.

The 2×2 transfer function matrix $T_{\text{des}}(s, \alpha)$ in (1-11) encodes a decoupled frequency and voltage control and relies on a grid-following signal causality, where the active and reactive power injection changes Δp and Δq are controlled as a function of the frequency and voltage magnitude measurements Δf and Δv . In line with that, we approximate the power grid at the interconnection terminals of the reserve unit, i.e., the point of common coupling (PCC), by a 2×2 small-signal dynamic equivalent $G(s)$, which describes the linearized power grid dynamics at the current steady-state operating point, and establishes the bus frequency and voltage magnitude deviations in response to the active and reactive power injections, i.e.,

$$\begin{bmatrix} \Delta f(s) \\ \Delta v(s) \end{bmatrix} = \underbrace{\begin{bmatrix} G_{11}(s) & G_{12}(s) \\ G_{21}(s) & G_{22}(s) \end{bmatrix}}_{=:G(s)} \begin{bmatrix} \Delta p(s) \\ \Delta q(s) \end{bmatrix}. \quad (1-10)$$

In particular, we assume that the grid operates at a fairly constant operating point, where the dynamics are nearly linear and time-invariant. In fact, during normal grid conditions, it is standard practice to build a small-signal model of the grid at a specific operating point to conduct analytical small-signal studies [39] or design adaptive controllers [40], which typically yields very accurate results. Moreover, since the dynamic model of the power system is typically not available in practice, we will use black-box identification methods to obtain the grid dynamic equivalent $G(s)$ in (1-10) from data. The procedure is outlined in the following subsection.

We aim to compute the optimal parameter vector α^* of the desired transfer function matrix $T_{\text{des}}(s, \alpha^*)$ which ensures an optimal and stable closed-loop performance of the interconnection in Figure 1-3, while satisfying (open-loop) grid-code and device-level requirements, i.e., the optimal parameter vector α^* within the parametric constraint set $\alpha \in \mathcal{G} \cap \mathcal{D}$, where $\mathcal{G} := \mathcal{G}^{\text{fcr}} \times \mathcal{G}^{\text{ffr}} \times \mathcal{G}^{\text{aux}} \times \mathcal{G}^{\text{vq}}$ and $\mathcal{D} := \left[\left[\mathcal{D}^{\text{fcr}} \times \mathcal{D}^{\text{ffr}} \times \mathcal{D}^{\text{aux}} \right] \cap \mathcal{D}^{\text{fp}} \right] \times \mathcal{D}^{\text{vq}}$ (with \times denoting the Cartesian product of sets). Our approach is based on a so-called “perceive-and-optimize” (P&O) strategy, which is composed of two main steps (see flow-chart in Figure 1-4) and elaborated in the following subsections, i.e.,

- “Perceive:” We first use the converter-based reserve unit to identify a grid dynamic equivalent $G(s)$ at its interconnection terminals via black-box identification methods.

- “Optimize:” We establish a closed-loop system interconnection of the identified $G(s)$ and the parametric transfer matrix $T_{des}(s, \alpha)$ as in Figure 1-3, where we optimize for the vector of transfer function parameters α^* which results in an optimal and stable closed-loop performance of the entire power grid response, while ensuring that grid-code and device-level requirements are reliably satisfied.

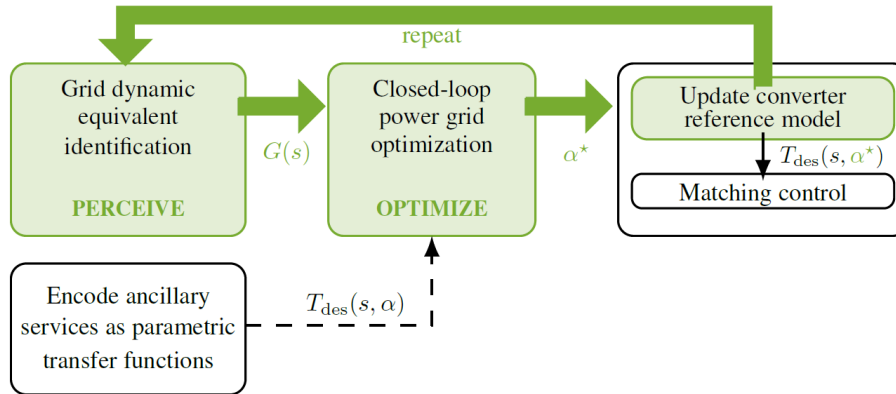


Figure 1-4 – Flowchart of the proposed “perceive-and-optimize” (P&O) approach for optimal dynamic ancillary services provision based on power grid perception.

During one P&O cycle, we assume that grid conditions remain unchanged. Specifically, the grid conditions during the perception step are assumed to coincide with those at which the optimal $T_{des}(s, \alpha^*)$ is applied, ensuring that the identified grid dynamic equivalent $G(s)$ accurately reflects the prevailing grid dynamics. In respect thereof, to address changing grid conditions, the two steps of the P&O strategy should be repeated regularly, e.g., in a quarterly or hourly fashion when the grid operating point is changing according to the day-ahead market [41]. Of course, also other (event-triggered or periodic) repetitions are possible. An investigation of such a multi-episodic application of the P&O strategy will be part of future work.

Remark 1. Although the assumptions of having linear time-invariant grid dynamics and unchanging grid conditions during one P&O cycle are idealized and rarely perfectly met in practice, it is important to notice that the feedback control structure of the P&O strategy effectively linearizes and enhances the system’s robustness in the face of model uncertainty.

1.2 Control Problem Formulation

The control of AGIs should be based on the topology of a given AGI. There are various AGI topological arrangements, and different topological configurations may require distinct control designs. Therefore, we first present typical AGIs’ modular topological arrangements and then provide a modular control design approach.

1.2.1 AGI Configurations

We first show four basic AGI configurations in Figure 0-3 with different coupling and terminal output types:

- AC-coupled AC-output topology, with separate DC-AC converters (and without a central converter);
- DC-coupled AC-output topology, with separate DC-DC converters and a central DC-AC converter;



- AC-coupled DC-output topology, with separate DC-AC converters and a central AC-DC converter;
- DC-coupled DC-output topology, with separate DC-DC converters and a central DC-DC converter.

Among these topologies, only the AC-coupled AC-output interface configuration has been explored in the literature [19] for the flexible aggregate GFM control. Recognizing the existence of all these topologies, we aim to explore generic modular configurations and control designs comprehensively.

Building on the basic modules, we can establish modular AC/DC hybrid grid interface configurations, an illustrative example of which is shown in Figure 0-4. There are n DERs connected at DC bus #0 in the top-level main interface. The aggregate i is represented by a collection of n_i DERs, which are connected to the main interface through a DC-coupled DC-output sub-interface at DC bus #1. Likewise, the aggregate j is represented by a collection of n_j DERs that are connected to the main interface through an AC-coupled DC-output sub-interface around AC bus #1. A large AC/DC hybrid interface can be assembled in such a modular way by encompassing multiple DC and AC coupling buses.

We highlight that a modular interface introduces a flexible and scalable approach to assembling AC and DC DERs. This modular grid interface offers many advantages, including but not limited to the following:

- High flexibility in achieving a desired dynamic behaviour;
- High scalability in modular configuration and control;
- Uniform standardization in enabling standardized protocols for multi-AC/DC-port interconnections;
- High transparency in understanding the dynamic behaviour of any bus from the interface level to the DER level.

1.2.2 Aggregate Grid-Forming Control

We consider a DC-coupled AC-output grid interface (which can arise as grid-connected DC microgrids) and formulate its control objectives. The control objectives of the other modules can be formulated similarly and will be summarized at the end of this subsection. For the DC-coupled AC-output module under consideration, its control objectives are illustrated in Figure 1-5, which comprise three parts: 1) the desired AC GFM response, 2) the AC-DC matching relationship, and 3) the DC contribution coordination.

- AC GFM

To provide a desired AC GFM dynamic behaviour¹, we specify the AC frequency and voltage response of the central inverter under AC-side power disturbances as

¹ We consider a grid-forming signal causality as a control objective, which is in contrast to the grid-following signal causality in (1-1). To address this, we can obtain a grid-forming signal causality by taking the inverse of (1-1).

$$\begin{bmatrix} \Delta f(s) \\ \Delta v(s) \end{bmatrix} = \begin{bmatrix} T_{\text{des}}^{\text{fp}}(s) & 0 \\ 0 & T_{\text{des}}^{\text{vq}}(s) \end{bmatrix} \begin{bmatrix} \Delta p(s) \\ \Delta q(s) \end{bmatrix}, \quad (1-11)$$

where Δp and Δq denote the active and reactive power output changes at the output terminal of the central inverter, and Δf and Δv denote the desired GFM response to the power disturbance. In the scope of dynamic ancillary services, we consider small-signal increment variables as the deviations of large-signal variables from their associated steady states or setpoints. The transfer functions in (1-11) can encode any desired linear/linearized responses in general such as virtual inertial response, damping, and steady-state droop relationship.

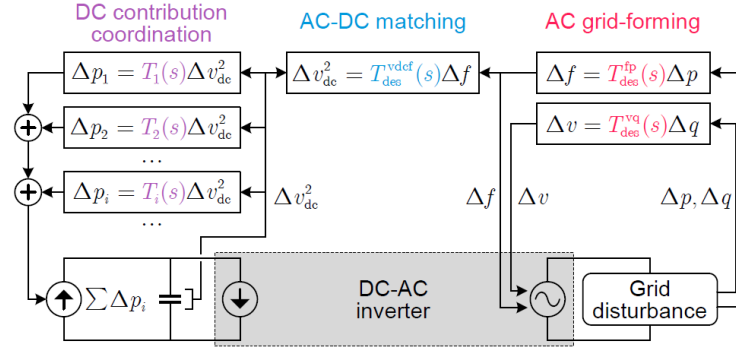


Figure 1-5 – Control objective sketch of a DC-coupled AC-output grid interface.

Remark 2. The desired dynamic response in (1-11) is specified by grid codes [42]. However, most current grid codes specify a desired dynamic response through piece-wise linear step-response capabilities curves in the time domain, rather than through a transfer function in the frequency domain. The latter, though, is preferable for control design and is more familiar to power electronics engineers. To obtain the transfer function corresponding to a dynamic response specification in a grid code, one can utilize the translation approach in [34]. Therefore, we assume that the desired transfer functions in (1-11) are given, which satisfy grid code requirements and respect the maximum capacity limitations of the DER aggregation [34].

- AC-DC Matching

A DC-coupled grid interface must maintain a stable and properly bounded DC-bus voltage to ensure normal operation. Inspired by the well-known matching control [43][44], to perform a DC-bus voltage forming behaviour, we specify an AC-DC matching relationship as,

$$\Delta(v_{\text{dc}}^2)(s) = T_{\text{des}}^{\text{vdcf}}(s)\Delta f(s), \quad (1-12)$$

where $\Delta(v_{\text{dc}}^2)$ denotes the variation of the DC voltage square² in response to the AC-side disturbance. The AC-DC matching in (1-12) thus specifies a desired relationship between the AC and DC ports of the inverter. The relationship not only facilitates the control design as shown in the next section but also offers a straightforward way to form the DC voltage and constrain its variation within an allowed range. More specifically, given an allowed variation range of the grid frequency, $|\Delta f|_{\text{max}}$, we can specify an appropriate $T_{\text{des}}^{\text{vdcf}}(s)$ such that the response of $|\Delta(v_{\text{dc}}^2)|$ is within an

² The reason for using voltage square, as in [43], is because power is linear in the square of voltage, simplifying the control design.



allowed variation range $|\Delta(v_{dc}^2)|_{\max}$.

Table 1-2 – Control objectives and control designs of the four basic grid interfaces

Grid interface type	AC-coupled AC-output	DC-coupled AC-output	AC-coupled DC-output	DC-coupled DC-output
Coupling type	AC	DC	AC	DC
Output type	AC	AC	DC	DC
Desired output behaviour	$\Delta f = T_{des}^{fp} \Delta p$	$\Delta f = T_{des}^{fp} \Delta p$	$\Delta p = T_{des}^{pvdc} \Delta(v_{dc}^2)$	$\Delta p = T_{des}^{pvdc} \Delta(v_{dc}^2)$
Desired matching between the coupling and output buses	$\Delta f = \Delta f$	$\Delta(v_{dc}^2) = T_{des}^{vdcf} \Delta f$	$\Delta(v_{dc}^2) = T_{des}^{vdcf} \Delta f$	$\Delta(v_{dc,1}^2) = T_{des}^{vdcvdc} \Delta(v_{dc}^2)$
Individual DER contribution	$\Delta f_i = T_i \Delta p_i$	$\Delta p_i = T_i \Delta(v_{dc}^2)$	$\Delta f_i = T_i \Delta p_i$	$\Delta p_i = T_i \Delta(v_{dc,1}^2)$
Aggregation condition	$\sum_i T_i^{-1} = T_{des}^{fp-1}$	$\sum_i T_i = T_{des}^{vdcf-1} T_{des}^{fp-1}$	$\sum_i T_i^{-1} = T_{des}^{vdcf} T_{des}^{pvdc}$	$\sum_i T_i = T_{des}^{vdcvdc-1} T_{des}^{pvdc}$

- DC Contribution Coordination

The desired GFM response ultimately relies on the power provision of DERs. To achieve the desired responses in (1-11) and (1-12), the control of DERs must be coordinated appropriately since heterogeneous DERs have different power response characteristics over time scales. In the frequency domain, the power response of each DER to a DC voltage variation is specified as

$$\Delta p_i(s) = T_i(s) \Delta(v_{dc}^2)(s), \quad (1-13)$$

where $T_i(s)$ represents the closed-loop control behaviour within each DER and $\Delta p_i(s)$ denotes the associated power output change. The specification of the control behaviour $T_i(s)$ should consider the following factors:

- The specification of $T_i(s)$ must respect the DER's characteristics. For example, a supercapacitor can only provide a dynamic response but not a steady-state contribution.
- For non-controllable DERs or user loads, their dynamics, captured by $T_i(s)$, are assumed to be fixed and known.
- The collective response of $T_i(s)$ should fulfill the desired AC GFM response in (1-11) and the AC-DC matching relationship in (1-12).

Analogously, we can specify the control objectives of the other grid interfaces, which are summarized in Table 1-2 and outlined in Appendix C. We highlight that the control objectives are interoperable between different interface modules, thus allowing the interconnection of multiple modules.

Finally, the control behaviours of all converters in a grid interface should be coordinated to satisfy the control objectives. A coordinated GFM control design will be presented to achieve the control objectives.

2 Optimal Dynamic Ancillary Services Provision

Our approach is based on a so-called “perceive-and-optimize” (P&O) strategy, which is composed of two main steps and elaborated in the following sections.

2.1 Grid Dynamic Equivalent Identification

Since the power grid is ever-changing and usually unknown from the perspective of a generation system, the grid dynamic equivalent $G(s)$ in (1-10) has to be measured online for a real-time assessment of the grid dynamics. To do so, for the reserve unit in Figure 0-2, we consider a grid-equivalent identification setup as in Figure 2-1(a), and resort to parametric¹ black-box grid impedance measurement techniques, as proposed in our prior work [45]. More specifically, employing such a black-box identification strategy enables us to identify the complete grid dynamic equivalent solely through measurement data collected at the interconnection terminal of the reserve unit, i.e., the complex and unknown grid dynamics can be accommodated without tailoring the model to specific system characteristics.

To identify $G(s)$ in (1-10), we inject uncorrelated wideband excitation signals with small perturbation levels (e.g., random binary sequences (RBS)) in the converter’s control loop of the reserve unit, to locally excite the system during online operation as in Figure 2-1(a). The resulting frequency and voltage magnitude responses, as well as the active and reactive power injections at the PCC, are then measured and collected as discrete-time samples to calculate an estimate of the grid dynamic equivalent $G(s)$. Figure 2-1(b) shows a block diagram of the identification problem, where the input/output perspective of the to-be-identified grid equivalent results from the electrical circuit equations.

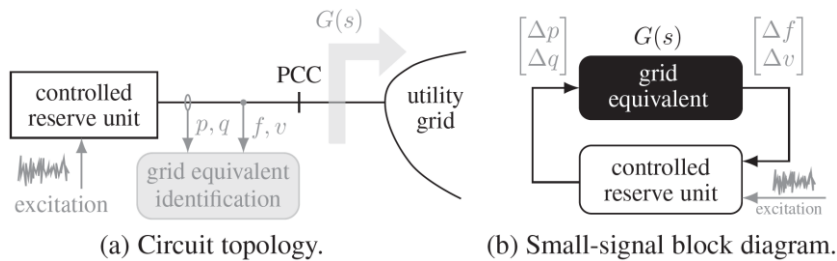


Figure 2-1 – Grid dynamic equivalent identification setup.

Given the collected input/output data, we can apply parametric³ system identification techniques such as prediction error methods (PEM) or subspace methods [45] to obtain an accurate estimate of the small-signal grid dynamic equivalent $G(s)$. Since PEM are typically simpler than subspace methods and can be computed very quickly, we consider them the preferred choice, especially for a multi-episodic application of the proposed P&O strategy. PEM works by minimizing the prediction error between the observed output of the system and the output predicted by the model. More specifically, the goal is to find model parameters that best capture the system’s dynamics, ensuring the model’s predictions are as accurate as possible. One of the simplest model structures used for

³ *Parametric* (i.e., model-based) system identification techniques directly identify an explicit system representation (e.g., a transfer function) and are not to be confused with *parametric* (i.e., parameter-dependent) transfer functions.

PEM is the so-called ARX (Auto-Regressive with eXogenous inputs) model. It represents a system's output as a linear combination of its previous outputs (auto-regressive part) and current and past inputs (exogenous part). The basic form of an ARX model is:

$$y(k) + a_1y(k-1) + \dots + a_ny(k-n) = b_1u(k-1) + \dots + b_mu(k-m) + e(k). \quad (2-1)$$

Here, $y(k)$ is the output at time step k , $u(k)$ is the input, a_i and b_j are the parameters to be estimated, and $e(k)$ is the prediction error. The simplicity of the ARX model lies in its straightforward linear relationship and ease of implementation, where the model parameters are estimated by solving a basic least-squares linear regression problem (for more details, see [45]).

Notice that in practical scenarios, measurement and process noise (e.g., external disturbances, inaccurate measurement devices) may be present during the grid dynamic equivalent identification. However, if the noise levels are not excessively high and a sufficient amount of data is collected, parametric system identification methods (especially PEM methods with a high-degree-of-freedom error model) can generally handle such noise and ensure that it only has minor impacts on the identification accuracy [46]. Larger noise levels, in turn, may necessitate special adjustments to the system identification methods [46][47]. For the practical setups in this work, however, the noise level is typically acceptable.

Remark 3. One may alternatively choose to first identify the grid impedance in other coordinates and then transform to polar coordinates as in (1-10) [48][49].

Remark 4. If the converter system has a small capacity compared to the power grid, it can only locally identify a "partial" grid equivalent in its vicinity, while the rest of the grid appears as an infinite bus. If so, the converter can only affect the grid dynamics during ancillary services provision in this vicinity.

2.2 Closed-Loop Power Grid Optimization

After identifying the grid dynamic equivalent $G(s)$, we now compute the optimal parameter vector α^* of $T_{des}(s, \alpha^*)$ which ensures an optimal and stable closed-loop performance of the interconnected system in Figure 1-3.

The α^* computation for the closed-loop system in Figure 1-3 can be recast as a system norm (input-output gain) minimization problem as in Figure 2-2, where we select a suitable performance index to be minimized. We translate both the grid dynamic equivalent $G(s)$ and the parametric transfer function matrix $T_{des}(s, \alpha)$ into a state-space system representation, where the control input of the former is given by the outputs of the latter (i.e., the active and reactive power deviations Δp and Δq). Moreover, to specify the closed-loop response behaviour, we define a weighted performance output z_p that has to be minimized when subject to some active and reactive power disturbance $w := [p_d, q_d]^T$. Namely, we consider z_p to be composed of the frequency deviation Δf , the rate-of-change-of frequency (RoCoF) $\Delta \dot{f}$, and the voltage deviation Δv , i.e.,

$$z_p = \left(r_f^{1/2} \Delta \dot{f}, r_f^{1/2} \Delta f, r_v^{1/2} \Delta v \right)^T, \quad (2-2)$$

where $r_{\dot{f}}, r_f, r_v$ are non-negative scalars trading off the relative deviations. If desired, further quantities of the closed-loop interconnection can be added to the performance output z_p , e.g., the

control efforts Δp and Δq . Since the latter, however, are already implicitly limited by the structural constraints on the parameter α , we refrain from including them into z_p .

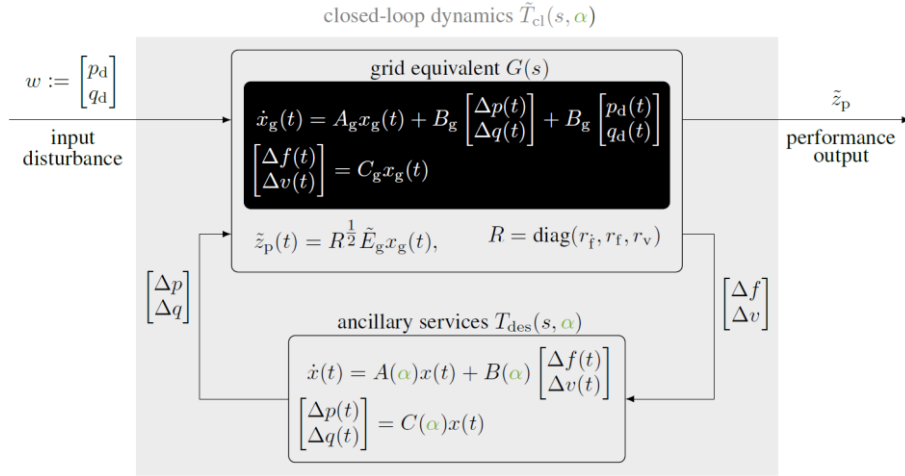


Figure 2-2 – Closed-loop interconnection for \mathcal{H}_2 optimization. The state vector x_g results from the extended state-space representation in (2-7) of the grid dynamic equivalent, which additionally outputs the approximate integral of Δf and Δv .

There exist different system norms (e.g., \mathcal{H}_2 or \mathcal{H}_∞) which provide a measure of the magnitude of the closed-loop system output z_p in response to the disturbance input w . In this work, we quantify the closed-loop system performance in terms of the \mathcal{H}_2 norm, which results in a computationally tractable and well-understood design problem, even for complex and large systems. Moreover, the \mathcal{H}_2 norm is generally considered a suitable proxy for typical power system specifications [7][8][9][50]. In particular, given that the \mathcal{H}_2 norm measures the energy of the system response to impulse disturbance inputs, we can replicate the closed-loop power system response to classical step disturbances, e.g., a sudden load increase or a generation drop, by considering the integral⁴ of the performance output in (2-2) as $\tilde{z}_p \approx \int z_p$ which, in the \mathcal{H}_2 norm, now reflects the system energy imbalance for *step-like* disturbances. Consequently, we define the cost function as

$$J = \int_0^\infty \tilde{z}_p^T \tilde{z}_p, \quad (2-3)$$

which corresponds to the squared \mathcal{H}_2 norm of the underlying closed-loop dynamical system $\tilde{z}_p = \tilde{T}_{cl}(s, \alpha)w$ between the disturbance input w and the performance output \tilde{z}_p as in Figure 2-2.

The closed-loop dynamical system $\tilde{z}_p = \tilde{T}_{cl}(s, \alpha)w$ can be obtained by closing the loop between the two state-space systems of $G(s)$ and $T_{des}(s, \alpha)$. More specifically, we consider the state-space representation⁵ of $T_{des}(s, \alpha)$ in (1-1) as

$$T_{des}(s, \alpha) = C(\alpha)(sI - A(\alpha))^{-1}B(\alpha), \quad (2-4)$$

⁴ We approximate the integral of $z_p = T_{cl}(s, \alpha)w$ as $\tilde{z}_p = \tilde{T}_{cl}(s, \alpha)w = 1/s + \epsilon T_{cl}(s, \alpha)w$, where ϵ is a small approximation factor of an ideal integrator, to ensure stability of $\tilde{T}_{cl}(s, \alpha)$ and the \mathcal{H}_2 norm to be well-defined [51].

⁵ $T_{des}(s, \alpha)$ and $G(s)$ can be ensured to be strictly proper by selecting the transfer function structure during grid-code translation & system identification.

where the associated differential equations are given as

$$\begin{aligned} \dot{x}(t) &= A(\alpha)x(t) + B(\alpha) \begin{bmatrix} \Delta f(t) \\ \Delta v(t) \end{bmatrix} \\ \begin{bmatrix} \Delta p(t) \\ \Delta q(t) \end{bmatrix} &= C(\alpha)x(t). \end{aligned} \quad (2-5)$$

To output the approximate integral $\tilde{z}_p \approx \int z_p$ of the performance output in (2-2), we consider an extended transfer function of $G(s)$ in (1-10) under the disturbance input $w = [p_d, q_d]^T$, i.e.,

$$\begin{aligned} \dot{x}(t) &= A(\alpha)x(t) + B(\alpha) \begin{bmatrix} \Delta f(t) \\ \Delta v(t) \end{bmatrix} \\ \begin{bmatrix} \Delta p(t) \\ \Delta q(t) \end{bmatrix} &= C(\alpha)x(t). \end{aligned} \quad (2-6)$$

where the associated state-space representation³ is given as

$$\begin{aligned} \dot{x}_g(t) &= A_g x_g(t) + B_g \begin{bmatrix} \Delta p + p_d \\ \Delta q + q_d \end{bmatrix} \\ \begin{bmatrix} \Delta f(s) \\ \Delta v(s) \\ \int \Delta f(s) \\ \int \Delta v(s) \end{bmatrix} &\approx \begin{bmatrix} C_g \\ C_g' \end{bmatrix} x_g(t), \end{aligned} \quad (2-7)$$

with the grid dynamic equivalent in (1-10) as

$$G(s) = C_g (sI - A_g)^{-1} B_g. \quad (2-8)$$

Finally, we can formulate the state-space representation of the resulting closed-loop dynamical system $\tilde{z}_p = \tilde{T}_{cl}(s, \alpha)w$ in Figure 2-2, i.e.,

$$\begin{aligned} \begin{bmatrix} \dot{x}_g \\ \dot{x}_{cl} \end{bmatrix} &= \underbrace{\begin{bmatrix} A_g & B_g C(\alpha) \\ B(\alpha) C_g & A(\alpha) \end{bmatrix}}_{=: A_{cl}(\alpha)} \underbrace{\begin{bmatrix} x_g \\ x \end{bmatrix}}_{=: x_{cl}} + \underbrace{\begin{bmatrix} B_g \\ O \end{bmatrix}}_{=: B_{cl}(\alpha)} w \\ \tilde{z}_p &= \underbrace{\begin{bmatrix} R^{1/2} \tilde{E}_g & O \end{bmatrix}}_{=: C_{cl}(\alpha)} \underbrace{\begin{bmatrix} x_g \\ x \end{bmatrix}}_{x_{cl}}, \end{aligned} \quad (2-9)$$

where $R := \text{diag}(r_{\tilde{p}}, r_f, r_v)$ and the matrix \tilde{E}_g results from the extended state-space representation in (2-7), which outputs Δf and the approximate integral of Δf and Δv , i.e.,

$$\tilde{E}_g = \begin{bmatrix} C_g[1, :] \\ C_g' \end{bmatrix}. \quad (2-10)$$

Finally, by recalling the constraints on α in (1-5), (1-6), (1-8), and (1-9), we can state the optimization problem to be solved for α^* as

$$\begin{aligned} &\underset{\alpha}{\text{minimize}} && J \\ &\text{subject to} && \dot{x}_{cl} = A_{cl}(\alpha)x_{cl} + B_{cl}(\alpha)w \\ & && \tilde{z}_p = C_{cl}(\alpha)x_{cl} \\ & && \alpha \in \mathcal{G} \cap \mathcal{D}, \end{aligned} \quad (2-11)$$

where $\mathcal{G} := \mathcal{G}^{\text{fcr}} \times \mathcal{G}^{\text{ffr}} \times \mathcal{G}^{\text{aux}} \times \mathcal{G}^{\text{vq}}$ and $\mathcal{D} := \left[\left[\mathcal{D}^{\text{fcr}} \times \mathcal{D}^{\text{ffr}} \times \mathcal{D}^{\text{aux}} \right] \cap \mathcal{D}^{\text{fp}} \right] \times \mathcal{D}^{\text{vq}}$ (with \times denoting the Cartesian product of sets). Due to the parametric nature of $A_{\text{cl}}(\alpha)$, $B_{\text{cl}}(\alpha)$ and $C_{\text{cl}}(\alpha)$, the problem in (2-11) is generally non-convex. However, since the objective function is smooth, an explicit gradient of J can be derived and directly used to solve the optimization problem via scalable first-order methods (e.g., projected gradient descent), similar as in [7][8][9][50]. A detailed computational approach to derive an expression for the gradient of J is presented in Appendix B.

The obtained desired transfer function matrix $T_{\text{des}}(s, \alpha^*)$ defines a frequency and voltage control behaviour in the frequency domain which can be realized in a converter-based generation system. More specifically, $T_{\text{des}}(s, \alpha^*)$ can be incorporated as a *reference model* into conventional cascaded converter control architectures which are designed for reference tracking, and thus enable a simple matching control implementation, e.g., via classical PI controllers. Moreover, such an implementation can handle changing reference models $T_{\text{des}}(s, \alpha^*)$ for different grid conditions with sufficient accuracy, such that a re-tuning of the PI gains is only needed in exceptional cases. Nevertheless, if one desires more advanced and robust matching control implementations, one could alternatively resort to multivariable linear parameter varying (LPV) \mathcal{H}_∞ methods [19][52], which can robustly include the time-varying parameter vector α , and hence directly account for time-varying grid conditions without re-computing the matching controller. However, the high-dimensionality and non-linear dependency of the parameters in $T_{\text{des}}(s, \alpha^*)$ might lack practical realizability of LPV methods.

Beyond that, instead of realizing $T_{\text{des}}(s, \alpha^*)$ with one single reserve unit, one might alternatively consider a heterogeneous collection of multiple energy sources (i.e., an AGI) to provide $T_{\text{des}}(s, \alpha^*)$ in aggregation [19][52]. This offers the advantage of providing dynamic ancillary services via $T_{\text{des}}(s, \alpha^*)$ across higher energy and power levels and a wider range of time scales, even during time-varying conditions of individual energy sources.

3 Aggregate Grid-Forming Control Design

This chapter presents a control design for a basic grid interface and then extends it to a modular grid interface.

3.1 Aggregation Condition for Distributed Energy Resources

To disaggregate the desired control objectives in (1-11) and (1-12) into the individual DER control behaviours in (1-13), we need first to aggregate the DER control behaviours. Based on (1-13), the aggregated power response on the DC bus is

$$\sum_{i=1}^n \Delta p_i(s) = \sum_{i=1}^n T_i(s) \Delta(v_{dc}^2)(s), \quad (3-1)$$

where there are n devices, including the controllable DERs (with DC-DC converters), non-controllable devices, and the DC capacitor (note that the capacitor also participates in the power response). For example, the dynamics of the DC capacitor C_{dc} is given as $T_c(s) = -\frac{1}{2}C_{dc}s$, with the negative sign complying with the sign convention of the output power. The power conservation between the DC and AC ports of the central inverter is represented as

$$\sum_{i=1}^n \Delta p_i(s) = \Delta p(s), \quad (3-2)$$

where we neglect the power losses in the DC network and converters. By plugging (3-1) and (3-2) into (1-11) and (1-12), we derive the following aggregation condition

$$\sum_{i=1}^n T_i(s) = T_{des}^{vdcf}(s)^{-1} T_{des}^{fp}(s)^{-1}. \quad (3-3)$$

It indicates the relationship in which the aggregated dynamics of the DC-side devices should satisfy the desired response.

For non-controllable devices, we account for their inherent dynamics as $T_i(s)$, e.g., the DC capacitor dynamics $T_c(s)$ shown earlier. We denote by \mathcal{N} the set of non-controllable devices and by \mathcal{C} the set of controllable DERs. Thus, the aggregation condition in (3-3) becomes

$$\sum_{i \in \mathcal{C}} T_i(s) + \sum_{i \in \mathcal{N}} T_i(s) = T_{des}^{vdcf}(s)^{-1} T_{des}^{fp}(s)^{-1}. \quad (3-4)$$

3.2 Coordinated Disaggregation of the Desired Behaviour

Based on the aggregation condition in (3-4), we disaggregate the desired response on the right-hand side of (3-4) appropriately, obtaining $T_i(s)$ for each controllable DER. To achieve this, we use dynamic participation factors similarly as for AC coupled-AC-output interfaces; see [52] for details. Briefly, we specify the contribution of each controllable DER, $T_i(s)$, $i \in \mathcal{C}$, as

$$T_i(s) := m_i(s) \left(T_{des}^{vdcf}(s)^{-1} T_{des}^{fp}(s)^{-1} - \sum_{i \in \mathcal{N}} T_i(s) \right). \quad (3-5)$$

The condition in (3-4) then simplifies to $\sum_{i \in \mathcal{C}} m_i(s) = 1$. For fast-acting DERs without steady-state

contribution, e.g., supercapacitors or flywheels, we can choose a high-pass filter for $m_i(s)$ to provide a fast dynamic response. For relatively slow DERs with steady-state contribution, e.g., renewable energy reserve units, we can choose a low-pass filter for $m_i(s)$ to provide power support on a longer time scale. For DERs covering the intermediate regime, e.g., battery energy storage systems, we can specify $m_i(s)$ as the residual part to fulfill the aggregation condition. The dynamic and steady-state participation can be adapted by tuning the time constant and static gain in $m_i(s)$. As in [52] for AC-coupled AC-output grid interfaces, the adaptation of the participation factors can be performed online in a centralized manner to account for the plugging-in and plugging-out of DERs and time-varying capacity limitations depending on weather conditions.

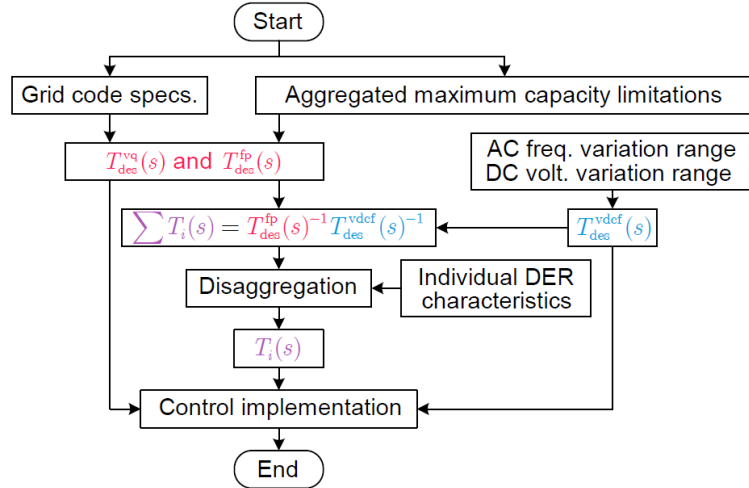


Figure 3-1 – Control design flowchart for a DC-coupled AC-output grid interface.

3.3 Implementable Local Control Strategies

The flowchart of the above control design is presented in Figure 3-1, where the procedure for obtaining desired control behaviours from the grid level to the local device level is shown. The obtained transfer function $T_{des}^{vdcf}(s)$ or $T_{des}^{fp}(s)$ will be used as frequency control specification of the central inverter, $T_{des}^{vq}(s)$ as voltage control specification of the inverter, and $T_i(s)$ as control specification of the DC-DC converters. An implementable control block diagram is shown in Figure 3-2.

- Inverter Control

The frequency control of the inverter can employ either $T_{des}^{vdcf}(s)$ or $T_{des}^{fp}(s)$ as the outer-loop controller, as shown in Figure 3-2, allowing two different implementations: A. AC-DC matching and B. AC p-f forming. The former uses the DC voltage while the latter uses the AC power as the feedback signal. More generally, one can also use their linear combination, which resembles a dual-port GFM control [25]. We recommend the AC-DC matching one between these two implementations since it does not require power setpoint coordination with the DC-DC converters. It also shows more robust DC voltage stability under large grid disturbances as it can self-balance the DC-bus power between the DER injection and the inverter output [44][53].

Compared to the frequency control, the voltage control of the inverter is simple (without need for DER coordination), which directly takes $T_{des}^{vq}(s)$ as the outer-loop controller, closing the loop between reactive power and voltage magnitude.

Given the resulting frequency reference f_{ref} and voltage magnitude reference v_{ref} from the outer-loop control outputs, the inner voltage and current loops can use proportional-integral (PI) controllers. One can replace the voltage PI controller with a virtual admittance and add a limiter for current limiting and fault ride-through under grid faults. The transient stability of the inverter can be further enhanced with an additional feedback loop of current saturation information, which can be found in [54], and is not included in Figure 3-2.

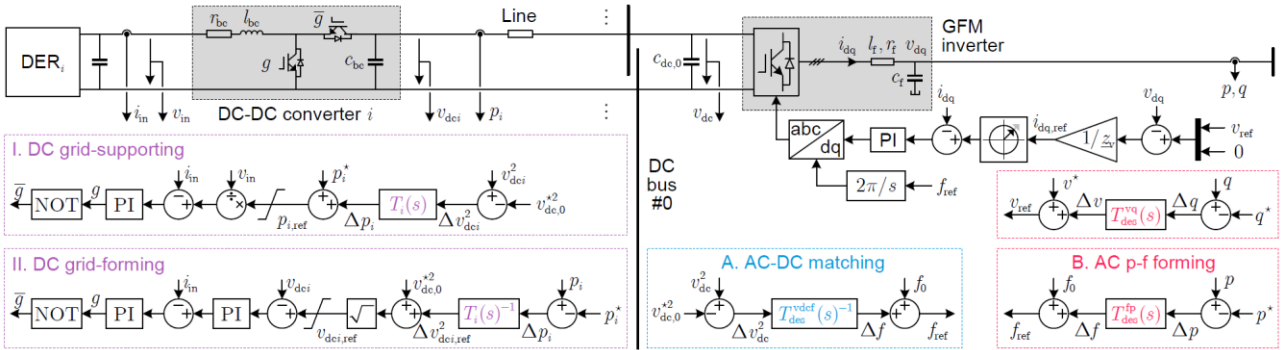


Figure 3-2 – Control block diagram of a DC-coupled AC-output grid interface, displaying two control implementation options for the inverter: A. AC-DC matching and B. AC p-f forming, and two control implementation options for the DC-DC converters: I. DC grid-supporting and II. DC grid-forming. Note that, the aggregation of $T_i(s)$ satisfies the condition in (3-3) concerning both $T_{des}^{vdcf}(s)$ and $T_{des}^{fp}(s)$ and therefore, the desired behaviour for both can be achieved, even though only one (i.e., option A or B) is implemented explicitly in the inverter, as the other one is achieved implicitly.

- DC-DC Converter Control

The control of the DC-DC converters also admits multiple implementations, two of which are shown in Figure 3-2: I. DC grid-supporting and II. DC grid-forming. The former, similar to classical AC grid-supporting control, measures the voltage variation and adjusts the power reference. The latter, resembling classical AC GFM control, measures the output power change and regulates the voltage reference. The desired control behaviour $T_i(s)$ and its inverse $T_i(s)^{-1}$ are used as the outer-loop controllers in the two implementations, respectively. Furthermore, limiting the power reference $p_{i,ref}$ and the voltage reference $v_{dc,i,ref}$ is crucial for the DC grid-supporting and DC grid-forming implementations, respectively, to prevent voltage collapse on the DER side during responses to large grid disturbances. Similar to the inverter, the inner voltage and current loops of the DC-DC converter can use PI controllers.

Remark 5. All transfer-function controllers to be implemented must be causal and stable. Since the desired grid interface response is stable, the disaggregated transfer functions are also stable. If a transfer function is non-causal, we can casualize it by adding a stable filter with a small time constant. During large disturbances, the output power of DERs or the inverter's output current may reach their limits due to the use of limiters. In such cases, the desired response cannot be fully achieved, but this trade-off is acceptable in practice since maintaining safety and stability is prioritized over grid support. Moreover, one can upgrade the PI controllers in the inner loops to more advanced controllers, such as \mathcal{H}_∞ control [52].

3.4 Extension to Modular AC/DC Hybrid AGIs

The control design for the four basic grid interfaces varies due to their different coupling and output types. Specifically, the main difference lies in their aggregation conditions while the disaggregation

and implementation are similar. For the DC-coupled AC-output interface, the aggregation condition is already given in (3-3). We derive the aggregation conditions for the other three modules in Appendix A and summarize their control designs in Table 1-2.

We extend the control design to modular interfaces as with the modular interface configuration. Since a modular interface can be assembled module by module, its control design can be developed in a systematic top-down approach, given the aggregation conditions for the individual interfaces. Consider the modular grid interface shown earlier in Figure 0-4 as an example. The top-down control design is outlined as follows.

- At the grid level, the desired AC GFM behaviour is specified as in (1-11).
- At the main-interface level, the control design for the DC-coupled AC-output module is based on the aggregation condition in (3-3) and the disaggregation in (3-5).
- At one sub-interface level, the control design for the DC-coupled DC-output module is based on the aggregation condition in (C-11) in Appendix A, which inherits the aggregate i 's desired control behaviour $T_i(s)$ as the desired output behaviour of this sub-interface.
- At another sub-interface level, the control design for the AC-coupled DC-output module is based on the aggregation condition in (C-5) in Appendix A, which inherits the aggregate j 's desired control behaviour $T_j(s)$ as the desired output behaviour of this sub-interface.
- Following the same way until we reach the bottom level, obtaining the desired control behaviour of each converter.

Remark 6. The top-down control design focuses on the AC-bus frequency and DC-bus voltage responses, requiring coordination among all AC and DC buses across converters. In contrast, the AC voltage response of AC buses can be controlled locally, without necessarily requiring coordination with other AC and DC buses, provided that the DC voltages of all DC-AC converters are already well regulated. For each AC bus in a modular grid interface, the voltage control for a desired response can be addressed using the same design as for an AC-coupled AC-output interface in [19].

4 Simulation Validations

4.1 Optimal Dynamic Ancillary Service Validation

To demonstrate the effectiveness of the proposed P&O approach, we use Simscape Electrical in MATLAB/Simulink to perform a detailed electromagnetic transients (EMT) simulation based on a *nonlinear* model of the three-phase two-area test system in Figure 4-1. In a first case study, we investigate how one single reserve unit, after applying the P&O strategy, can significantly improve the overall closed-loop power grid performance during nominal grid conditions, while satisfying grid-code and device-level requirements. For the same setup, we additionally run Monte Carlo simulations to investigate how an inaccurate grid dynamic equivalent model during changing grid conditions is affecting the effectiveness of the P&O strategy. In a second case study, we consider oscillatory grid conditions caused by weakly-damped inter-area modes, and reveal how a sequential application of the P&O strategy by multiple reserve units allows us to iteratively optimize the overall frequency and voltage response behaviour of the power grid while attenuating the inter-area oscillations.

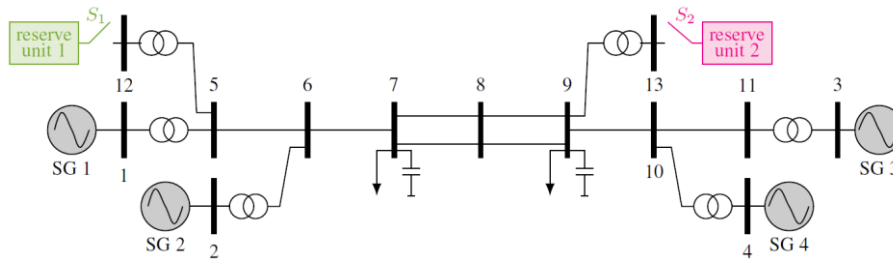


Figure 4-1 – One-line diagram of the three-phase two-area test system with two converter-based reserve units for optimal dynamic ancillary services provision.

4.1.1 Simulation Setup

The two-area system in Figure 4-1 consists of two areas connected by a weak tie. It contains four thermal-based synchronous generators (SGs) and two additional converter-based reserve units connected to buses 12 and 13. The transmission lines are modelled via nominal π sections (i.e., with RLC dynamics), and the step-up transformers via three-phase linear models. We adopt an 8th-order model for the synchronous machines equipped with an IEEE type 1 voltage regulator (AVR) combined with an exciter, and a power system stabilizer (PSS). The governors are modeled as a proportional speed-droop control with first-order delay, and the turbines as reheat steam turbines [55]. The power grid parameters are chosen similarly as in [55], and the main parameters of the SGs are summarized in Table 4-1.

We use a converter to represent a single reserve unit in validating the optimal dynamic ancillary services. The optimal dynamic services can also be readily applied to an AGI with multiple DERs. The proposed grid-side converter model is shown in Figure 4-2 with the associated parameters in Table 4-2. It represents an aggregation of multiple commercial converter modules and is based on a state-of-the-art converter control scheme [56]. We can easily incorporate the required grid dynamic equivalent identification setup and the transfer-function matching control in such a setting. While Figure 4-2 shows only one exemplary converter control architecture, our method is compatible with any control architecture that accepts active and reactive power references.



Table 4-1 – Main parameters of the SGs in the nominal two-area system.

Parameter	Value	Parameter	Value
SG power rating	900 MVA	Exciter gain	200
SG voltage rating	20 kV	Exciter time const.	0.001 s
Governor droop gain	0.05	PSS gain	25
Governor time constant	0.2 s	PSS wash-out time const.	1 s
Steam chest time constant	0.5 s	Lead-lag time const. # 1	50e-3 s, 20e-3 s
Turbine power fraction	0.3	Lead-lag time const. # 2	3 s, 5.4 s
Reheat time constant	8 s	Equivalent inertia	4 s (SG 1&2) 4.35 s (SG 3&4)

Table 4-2 – Converter parameters of reserve units 1 and 2.

Parameter	Symbol	Value
Voltage, power & frequency base	V_b, S_b, f_b	1 kV, 500 MVA, 50 Hz
DC-link capacitor	C_{dc}	0.24 p.u.
RL-filter components	L_f, R_f	0.1 p.u., 0.01 p.u.
DC-source time constants	$\tau_{dc,1}, \tau_{dc,2}$	0.1 s, 0.04 s
Norm. max. active power ramp. rate	$R_{max,1}^p, R_{max,2}^p$	111 s ⁻¹ , 150 s ⁻¹
Norm. max. reactive power ramp. rate	$R_{max,1}^q, R_{max,2}^q$	150 s ⁻¹ , 150 s ⁻¹
Norm. max. active power peak capac.	$M_{max,1}^p, M_{max,2}^p$	70, 100
Max. FFR support duration	$t_{d,max,1}^{ffr}, t_{d,max,2}^{ffr}$	20 s, 20 s
Max. return-to-recovery time	$t_{r,max,1}^{ffr}, t_{r,max,2}^{ffr}$	20 s, 20 s

Similar to [57], we assume the dc current i_{dc} to be supplied by a controllable dc current source, e.g., schematically representing the machine-side converter of a direct-drive wind turbine, a PV system, etc. In particular, we consider a generic coarse-grain model of the primary source and model its response time by a first-order delay with a time constant τ_{dc} [57] e.g., representing the dynamics of the resource as well as communication and/or actuation delays. Further, we limit the primary source input by a saturation element, which, e.g., corresponds to the power/current limits of a machine-side converter or an energy storage system, or PV/wind power generation limits. For wind or PV generation, we assume that they are operated under deloaded conditions with respect to their maximum power point, allowing them to put an active power reserve aside for participating in frequency regulation. While we stick to such an abstract representation of the primary source, one could also consider more detailed models tailored to the application at hand.

The ac-side control of the grid-side converter is used to control the output current magnitude. It is implemented in a dq-coordinate frame generated via a phase-locked loop (PLL), which tracks the system frequency to keep the converter synchronized with the grid voltage [56].

To identify the grid dynamic equivalent $G(s)$, we inject uncorrelated wideband excitation signals with small perturbation levels in the converter’s control loop to excite the power grid during online operation as indicated in Figure 4-2. The resulting frequency and voltage magnitude responses, as well as the active and reactive power injections at the PCC are then measured and collected in the form of discrete-time samples to calculate an estimate of the grid dynamic equivalent $G(s)$.

Finally, the transfer function matching control is included in the outer control loop of the converter via simple PI controllers to track the desired dynamic response behaviour for frequency and voltage

regulation as $T_{des}^{fp}(s, \alpha^*)$ and $T_{des}^{vq}(s, \alpha^*)$, respectively.

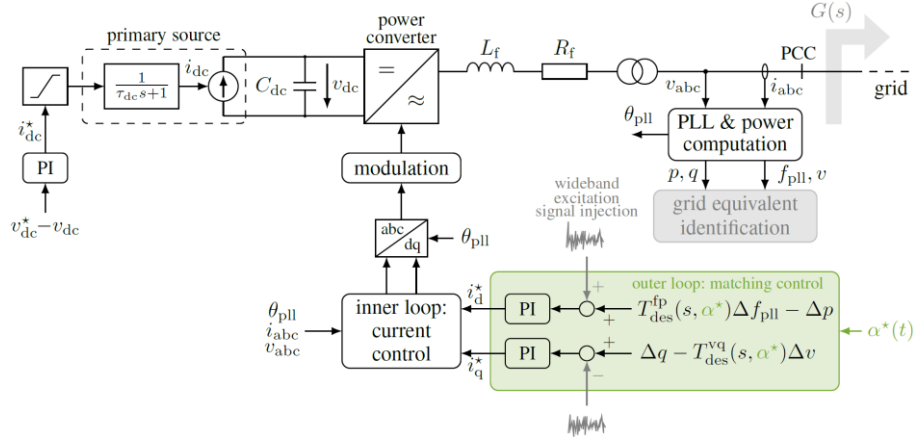


Figure 4-2 – One-line diagram of three-phase power converter interface of one reserve unit including grid equivalent identification and matching control.

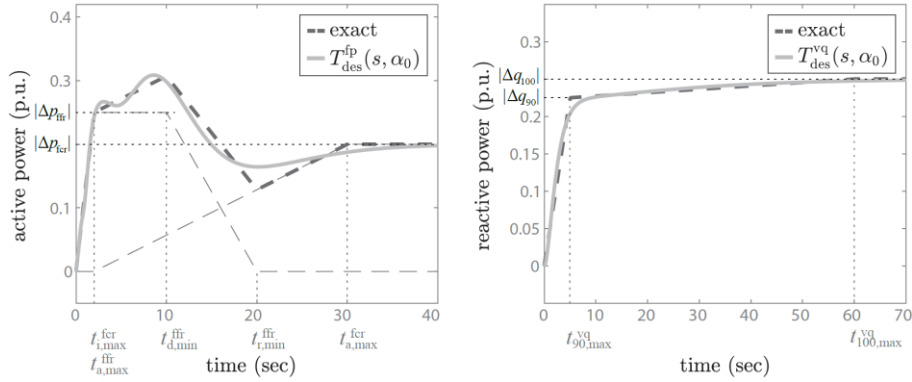


Figure 4-3 – Active and reactive power response after a negative frequency and voltage step change for the cheap $T_{des}(s, \alpha_0)$ which satisfies minimal grid-code requirements (cf. grid-code examples in Figure 1-1 and Figure 1-2).

To demonstrate the efficiency of the proposed P&O strategy in the following case studies, we define a *cheap* desired transfer function matrix $T_{des}(s, \alpha_0)$ as a benchmark ancillary services specification to compare with. More specifically, we select α_0 as the critical point within \mathcal{G} where all grid-code constraints in Appendix B are active, i.e.,

$$\begin{aligned}
 \text{FCR: } & t_i^{fcr} = t_{i,max}^{fcr}, \quad t_a^{fcr} = t_{a,max}^{fcr} \\
 \text{FFR: } & t_a^{ffr} = t_{a,max}^{ffr}, \quad t_d^{ffr} = t_{d,min}^{ffr}, \quad t_r^{ffr} = t_{r,min}^{ffr}, \quad x^{ffr} = 1 \\
 \text{AUX: } & m_{aux} = 0 \\
 \text{VQ: } & t_{90}^{vq} = t_{90,max}^{vq}, \quad t_{100}^{vq} = t_{100,max}^{vq},
 \end{aligned} \tag{4-1}$$

thereby encoding the *minimum* open-loop grid-code requirements as in Table 1-1. In particular, such a basic choice of α_0 results in a cheap, but feasible dynamic ancillary services provision, where the effort of the reserve unit is pared down to the minimum. The active and reactive power responses of the cheap control $T_{des}(s, \alpha_0)$ (and the underlying piece-wise linear time-domain curves) after a frequency and voltage step change are depicted in Figure 4-3. The associated active and reactive power capacity levels are fixed by the allocated active and reactive power droop gains $D_p = -0.05$, $K_p = -0.04$ and $D_q = -0.04$ (cf. Figure 1-1 and Figure 1-2(b)). Notice that we will use the same droop gains also for the optimal $T_{des}(s, \alpha^*)$ computation in the following case studies,

since they are typically directly given by the system operator and might not allow for flexibility.

4.1.2 Case Study C: Nominal Grid Conditions

We commence our validation by examining nominal grid conditions, where only reserve unit 1 is interconnected with the two-area system (S1 closed in Figure 4-1), while reserve unit 2 remains disconnected (S2 open). As a starting point, we consider the cheap transfer function matrix $T_{des,1}(s, \alpha_0)$ to be realized in the outer loop of the converter system of reserve unit 1. Based on this, we aim to improve the overall closed-loop power grid performance by applying the P&O strategy to compute an optimal $T_{des,1}(s, \alpha_{nom}^*)$ for reserve unit 1.

- Grid Dynamic Equivalent Identification

We use the converter interface of reserve unit 1 to identify the grid dynamic equivalent $G_1(s)$ as in Figure 4-4. During the online grid identification experiment, we consider constant stationary grid conditions. To excite the power grid, we inject two uncorrelated superimposed RBS signals, each with an amplitude of 0.03 p.u. and a sampling rate of 1 kHz, in the power loop of the converter control architecture in Figure 4-2 for 40 seconds. When doing so, we ensure that the perturbation level is rather small to not deteriorate the ongoing grid operation.

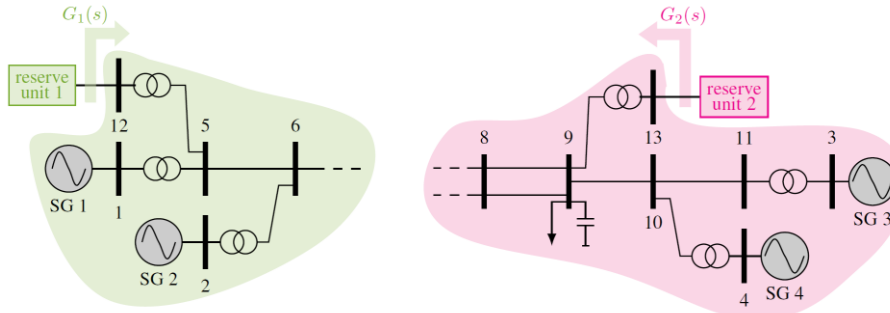


Figure 4-4 – Grid dynamic equivalent identification of the two-area system.

The small-signal frequency and voltage magnitude responses, as well as the active and reactive power injections at the PCC of reserve unit 1, are then measured and collected (in the presence of measurement noise) at a sampling rate of 1 kHz. Since the recorded data set is based on discrete-time samples, the parametric grid impedance model is (initially) identified in the discrete domain. Namely, following a similar procedure as in [45], we compute an ARX model by applying parametric system identification techniques. We additionally include other processing steps (e.g., prefiltering of the data) to ensure the accuracy of the system identification in the frequency range of interest. A proper model structure and order selection is done iteratively by testing a certain model structure and order and checking the fitting performance with some validation data. Once an appropriate ARX transfer function model has been identified, we apply model reduction techniques and convert it from discrete into continuous domain to finally obtain $G_1(s)$ of order 17. The resulting Bode diagram of $G_1(s)$ is illustrated by the solid green line in Figure 4-5. We can see that an accurate fitting of the reference grid model (obtained via *noise-free* sinusoidal sweep methods and indicated by the star symbols) is achieved.

- Optimal T_{des} Computation

Once the dynamic grid equivalent $G_1(s)$ is identified, we proceed to solve the closed-loop power

grid optimization problem, to compute a locally optimal solution for α_{nom}^* , while taking both grid-code and local device-level limitations of reserve unit 1 into consideration. It is crucial to note that $G_1(s)$ is a full 2×2 matrix, therefore capturing the inherent coupling of active and reactive power with both frequency and voltage during closed-loop optimization. The resulting optimal parameter vector α_{nom}^* is presented in Table 4-3. A comparative analysis of the open-loop step response behaviours of the optimal $T_{des,1}(s, \alpha_{nom}^*)$ and the cheap $T_{des,1}(s, \alpha_0)$ in Figure 4-6 allows us to conclusively assess the reliable satisfaction of minimum grid-code requirements of $T_{des,1}(s, \alpha_{nom}^*)$. Finally, by realizing the obtained $T_{des,1}(s, \alpha_{nom}^*)$ in the converter control loop of reserve unit 1, we observe a significant enhancement of the closed-loop system response behaviour. Namely, despite being bandwidth and capacity-limited, and with only half the rating of one SG, the optimal dynamic ancillary services provision by reserve unit 1 demonstrates a substantial improvement of the system response during a load increase at bus 7 (Figure 4-7). Specifically, we achieved a **12.6%** improvement in the rate of change of frequency (RoCoF), an **11.6%** improvement in frequency nadir, and a **32.9%** reduction in voltage peak compared to the initial cheap $T_{des,1}(s, \alpha_0)$ implementation.

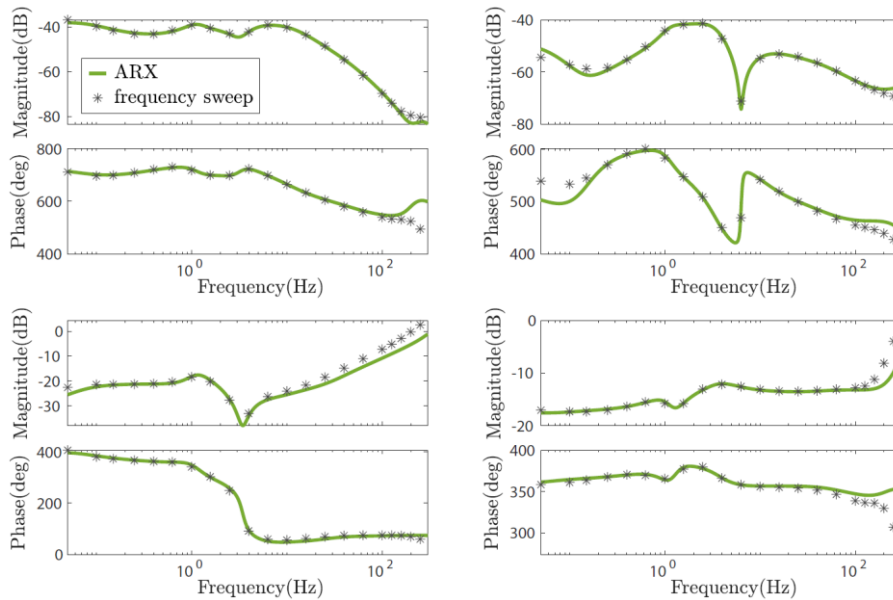


Figure 4-5 – Bode diagrams of the identified 2×2 grid dynamic equivalent $G_1(s)$ for the nominal two-area system in Figure 4-4(a).

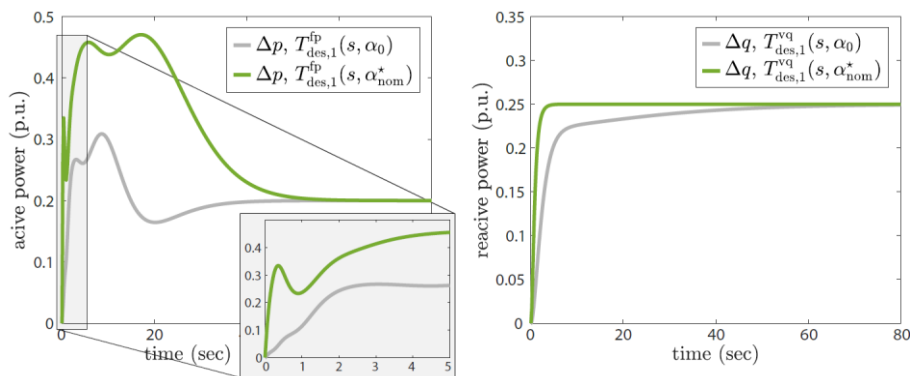


Figure 4-6 – Open-loop active and reactive power step responses after a negative frequency and voltage step change for the optimal $T_{des,1}(s, \alpha_{nom}^*)$ and the cheap $T_{des,1}(s, \alpha_0)$, respectively.

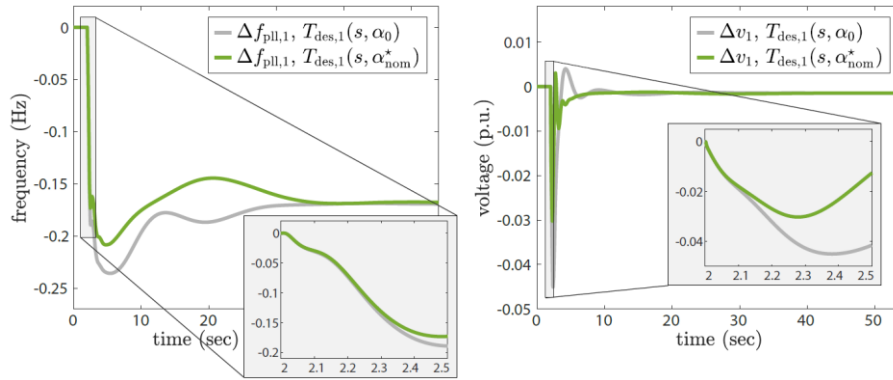


Figure 4-7 – Closed-loop system response behaviour of the nominal two-area system after a load increase at bus 7 for the optimal $T_{des,1}(s, \alpha_{nom}^*)$ and the cheap $T_{des,1}(s, \alpha_0)$, respectively.

- Changing Grid Conditions

Given the exceptional performance of the optimal $T_{des,1}(s, \alpha_{nom}^*)$ under “laboratory conditions”, we now aim to investigate the effectiveness of the proposed P&O strategy when dealing with inaccurate grid dynamic equivalent models. Possible sources of model inaccuracy include scenarios where the grid is not operating in a small-signal regime, changes in grid conditions after identifying the grid dynamics during one P&O cycle, or significant identification errors caused by high noise levels during system identification. In the following, we exemplarily investigate changing grid conditions after the grid identification during one P&O cycle as one possible source of model inaccuracy.

To further this investigation, we apply the previously obtained optimal $T_{des,1}(s, \alpha_{nom}^*)$ to various grid conditions that differ from those initially perceived in Figure 4-5. More specifically, we perform Monte Carlo simulations by applying random active power generation set points to the four SGs in the 2-area system, varying within a range of $\pm 10\%$ from the nominal scenario, and study the system’s response behaviour during the same load increase at bus 7 as before. The simulation results, illustrated in Figure 4-8, reveal that even with an inaccurate grid dynamic equivalent model, the P&O strategy enhances the overall system response with close to optimal performance. This demonstrates the robustness of the P&O strategy against minor inaccuracies in dynamic grid equivalent models. Nevertheless, the suboptimal response at the same time also highlights the necessity for accurate grid models, which can be achieved by reducing identification and model errors due to noise, or by adopting a multi-episodic application of the P&O strategy where grid dynamics are continuously updated online in response to significantly changing grid conditions.

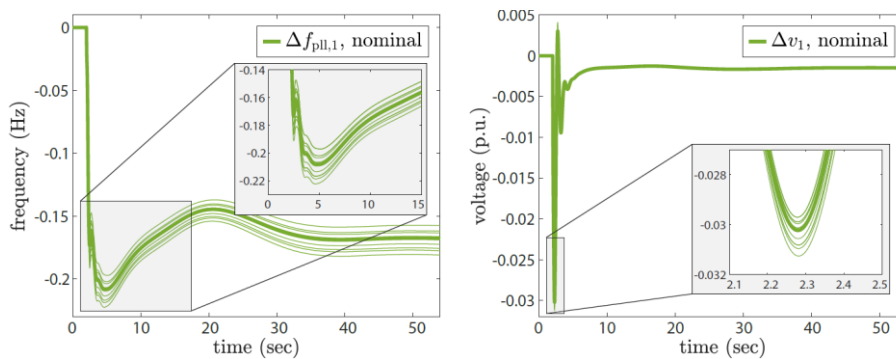


Figure 4-8 – Closed-loop response behaviour of the two-area system following a load increase at bus 7, analysed for the optimal $T_{des,1}(s, \alpha_{nom}^*)$ in a nominal scenario (fat curve) and in Monte Carlo simulations with

randomly varied active power generation set points of the SGs within a $\pm 10\%$ range (thin curves).

4.1.3 Case Study D: Oscillatory Grid Conditions with Multiple Reserve Units

We now consider oscillatory grid conditions caused by weakly-damped inter-area modes, arising from long transmission lines, fast exciters, and ill-tuned PSS gains (we decreased the PSS gains by a factor of five). Both reserve units are connected to the 2-area system (S1 and S2 closed), initially providing ancillary services as specified by the cheap transfer function matrices $T_{des,1}(s, \alpha_0)$ and $T_{des,2}(s, \alpha_0)$, respectively. Being limited in energy, reserve unit 2, does not provide the FCR service, i.e., we eliminate the $T_{des,2}^{fcr}$ term in (1-3).

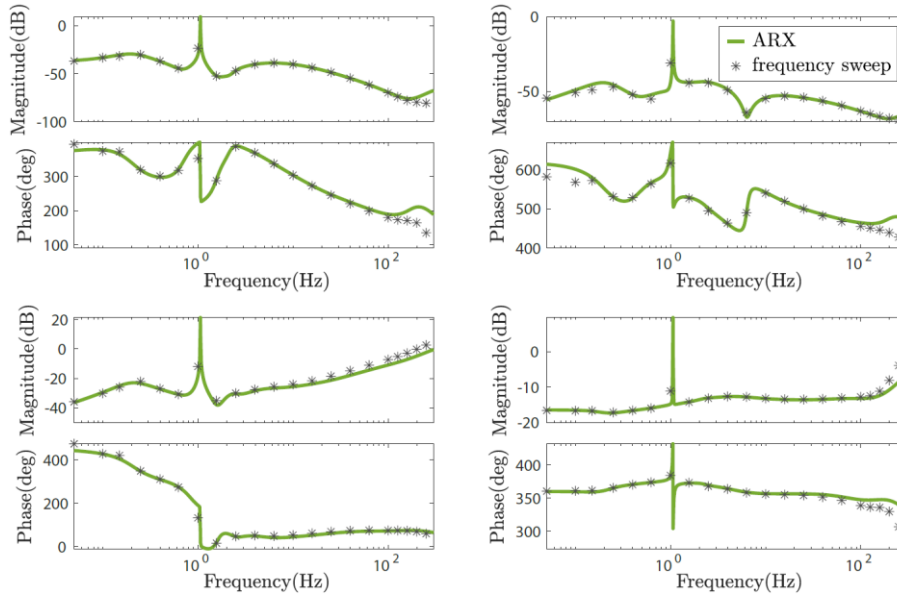


Figure 4-9 – Bode diagrams of the identified 2×2 grid dynamic equivalent $G_1(s)$ for the oscillatory two-area system in Figure 4-4(a) during the first P&O cycle.

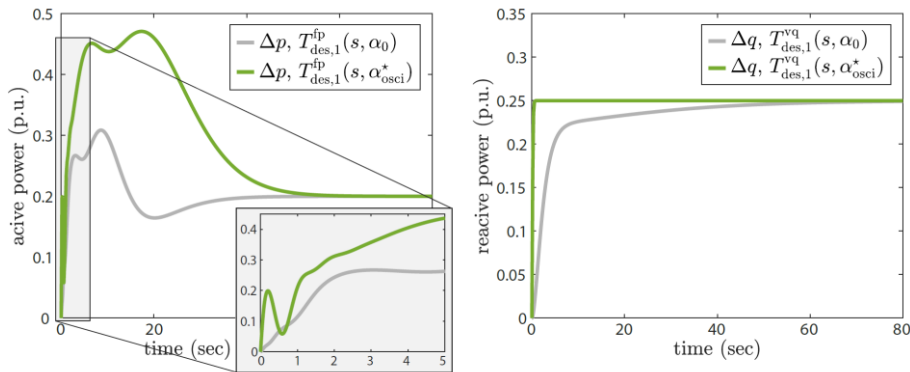


Figure 4-10 – Open-loop active and reactive power step responses after a negative frequency and voltage step change for the optimal $T_{des,1}(s, \alpha_{osci}^*)$ and the cheap $T_{des,1}(s, \alpha_0)$, respectively.

Related to our earlier discussion, we study a multi-converter scenario of the proposed method for optimal dynamic ancillary services provision, where each reserve unit applies the P&O strategy sequentially, while the remaining units stay connected with their previous $T_{des,i}(s, \alpha^*)$.

- First P&O Cycle

During grid identification, we obtain $G_1(s)$ of order 20. The resulting Bode diagram is illustrated by

the solid green line in Figure 4-9, with a significant resonance peak at approximately 1 Hz, indicating the oscillation frequency of the weakly-damped inter-area modes of the two-area system.

For identical cost-function weights and gradient descent algorithm settings as in case study I, we compute an optimal α_{osci}^* as listed in Table 4-3. The associated open-loop step response of $T_{\text{des},1}(s, \alpha_{\text{osci}}^*)$ is depicted in Figure 4-10. By comparing α_{osci}^* with the optimal α_{nom}^* from the previous case study I during nominal grid conditions, it becomes apparent how different grid conditions generally result in a different optimal dynamic ancillary services provision (for the same optimization settings).

Table 4-3 – Optimal transfer function parameters α^* for case studies C and D.

	t_i^{fcr}	t_a^{fcr}	t_a^{ffr}	t_d^{ffr}	t_r^{ffr}	χ^{ffr}	ω_l	ω_h	m_{aux}	t_{90}^{vq}	t_{100}^{vq}
α_0	2	30	2	10	20	1	-	-	0	5	60
α_{nom}^*	0.01	3.73	1.32	21.32	41.32	1	2.4	7	-43.15	1.56	2.87
$\alpha_{\text{osci}}^* \#1$	0.01	5.64	1.65	21.65	41.65	1	5.36	9.96	-40.16	0.29	0.3
$\alpha_{\text{osci}}^* \#2$	-	-	0.84	20.84	40.84	1.35	0.95	5.55	-64	0.48	1.27

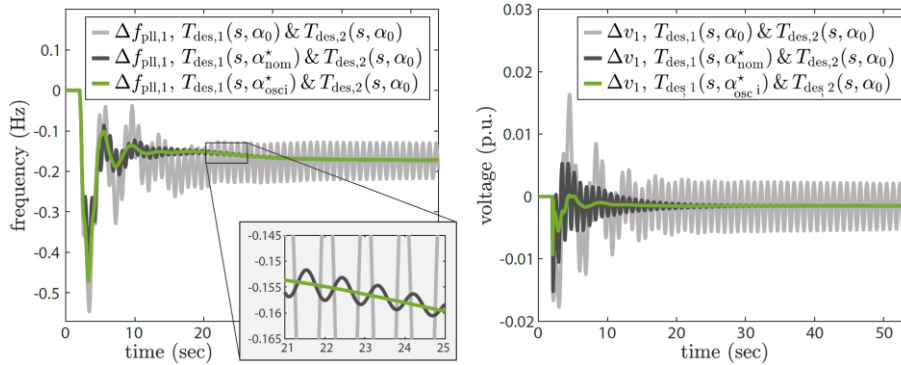


Figure 4-11 – Closed-loop system response behaviour of the oscillatory two-area system after a load increase at bus 7. We compare the optimal $T_{\text{des},1}(s, \alpha_{\text{osci}}^*)$, the nominal $T_{\text{des},1}(s, \alpha_{\text{nom}}^*)$, and the cheap $T_{\text{des},1}(s, \alpha_0)$, of reserve unit 1, respectively. Reserve unit 2 is always realizing the cheap $T_{\text{des},2}(s, \alpha_0)$.

With $T_{\text{des},1}(s, \alpha_{\text{osci}}^*)$, we can improve the oscillatory closed-loop system response of the two-area system quite significantly, i.e., once again, the performance enhancement of α_{osci}^* over α_0 is astonishing. As illustrated in Figure 4-11, the inter-area oscillations at 1 Hz are significantly attenuated during a load increase at bus 7. Moreover, compared to the system response with the cheap $T_{\text{des},1}(s, \alpha_0)$, we can achieve a **10.5%** improvement in RoCoF, a **13.8%** improvement in frequency nadir, and a voltage peak reduction of **47.5%**. Finally, the optimal $T_{\text{des},1}(s, \alpha_{\text{nom}}^*)$ for nominal grid conditions in case study I does not result in a satisfying response behaviour when deployed in the oscillatory grid, which, in alignment with our observations during the Monte Carlo Simulations, justifies the necessity of perceiving the grid characteristics in an online manner, especially during significantly changing grid conditions.

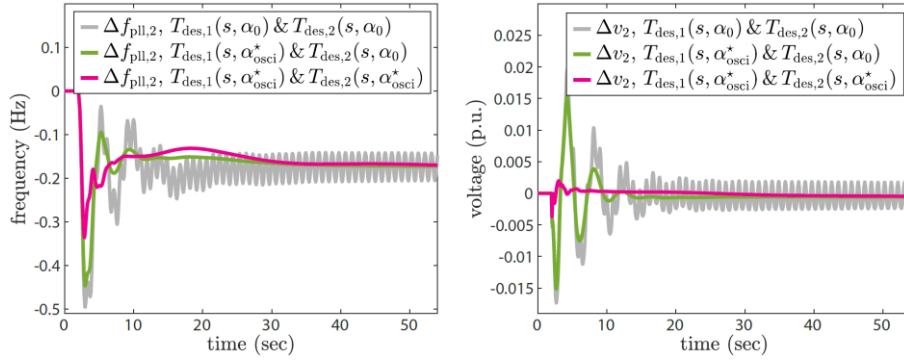


Figure 4-12 – Closed-loop system response behaviour of the oscillatory two-area system after a load increase at bus 7. We compare the initial system configuration based on the cheap $T_{des,1}(s, \alpha_0)$ and $T_{des,2}(s, \alpha_0)$ of both units, with the optimal $T_{des,1}(s, \alpha_{osci}^*)$ of unit 1 after the first P&O cycle and the optimal $T_{des,2}(s, \alpha_{osci}^*)$ of unit 2 after the second P&O cycle.

- Second P&O Cycle

Keeping $T_{des,1}(s, \alpha_{osci}^*)$ for reserve unit 1, we now apply the P&O strategy to reserve unit 2. After a grid identification as in Figure 4-4, we obtain $G_2(s)$ of order 24 and compute the optimal $T_{des,2}(s, \alpha_{osci}^*)$ with α_{osci}^* as in Table 4-3. Compared to the first P&O cycle, we can clearly observe a further improvement of the overall closed-loop grid response behaviour during a load increase at bus 7 (Figure 4-12), i.e., a RoCoF improvement of **16.1%**, a frequency nadir improvement of **24.7%**, and a voltage peak improvement of **75.9%**.

Remark 7. The proposed P&O strategy is fully decentralized, as each grid-connected reserve unit executes its own perceive-and-optimize cycle independently. Consequently, the computational complexity of each P&O iteration does not increase with the number of connected units, ensuring intrinsic scalability. The only open point for future investigation concerns the simultaneous activation of multiple units, since in this deliverable we adopt an initial iterative scheme as a naïve multi-unit coordination mechanism. Regarding implementation requirements, the method only necessitates an excitation signal injection within each converter’s control loop and standard measurement equipment at the PCC for identifying the local grid dynamic equivalent.

4.2 Aggregate Control Performance Validation

This section presents case studies to validate the performance of the proposed control design. The simulation system setup is shown in Figure 4-13. In case study A, a grid interface is connected to an infinite-bus system to test whether it can achieve the desired response. The infinite-bus setup is used to impose an intended change in grid frequency and voltage that complies with the test requirements of grid codes [34]. In case study B, we connect the grid interface to the IEEE 13-bus distribution system [58] to test its performance under more realistic load disturbances and short-circuit faults. The case studies employ high-fidelity simulation models of DC-AC and DC-DC converters, in which their inner voltage and current loops, PWM modulation, and IGBT switches are included. Open-source simulation models are available at <https://github.com/Xiuq-He/grid-interface>. The main system parameters can be found in Table 4-4.

4.2.1 Simulation Setup

The desired aggregate response is represented in per-unit as follows, where we omit “(s)” for

brevity, similarly hereafter,

$$T_{des}^{fp} = \frac{-1}{5s + 25}, \quad T_{des}^{vq} = \frac{-0.2}{0.01s + 1}, \quad T_{des}^{vdcf} = 10, \quad (4-2)$$

with minus signs indicating negative feedback droop, an inertia time constant 5 s, a typical frequency droop slope $1/25 = 4\%$, and a typical voltage droop slope 20%. Moreover, the desired AC-DC matching relationship T_{des}^{vdcf} suggests that a 10 % DC voltage-square variation will accompany a 1% frequency variation. Note that the desired response in (4-2) can also be chosen to represent more diverse grid code requirements or to achieve optimal dynamic ancillary services.

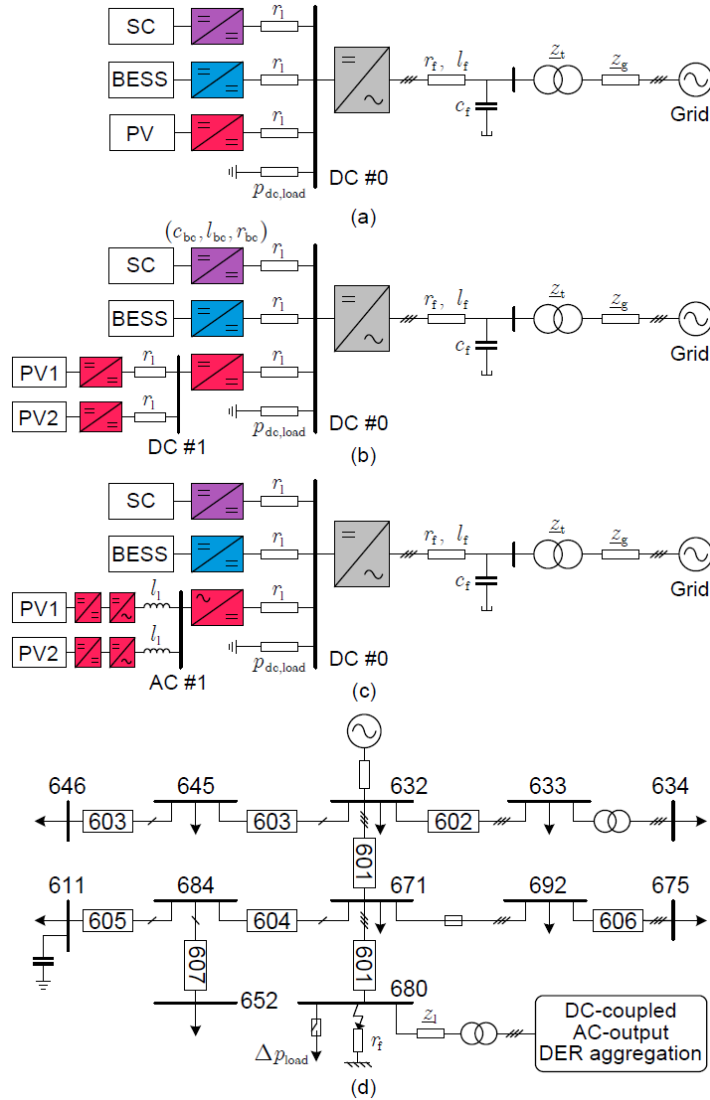


Figure 4-13 – Illustration of the system setup in case studies. (a) A basic DC-coupled AC-output grid interface. (b) A multi-DC-bus interface. (c) An AC/DC hybrid interface. (d) A DC-coupled AC-output grid interface connected to the IEEE 13-bus system.

Table 4-4 – Parameters in simulation validations of AGI dynamic performance.

Symbol	Description	Value
s_N	AGI nominal capacity	1 MVA
ω_0	Fundamental frequency	120π rad/s
v_N	AC nominal voltage (ph-ph, rms)	400 V
$v_{dc,0}^*$	DC bus #0 nominal voltage	800 V



$v_{dc,1}^*$	DC bus #1 nominal voltage	480 V
\underline{z}_g	Grid impedance	$0.08 + j0.4$ p.u.
\underline{z}_l	Line impedance	$0.07 + j0.2$ p.u.
\underline{z}_t	Transformer impedance	$0.002 + j0.06$ p.u.
l_f	Filter inductance	0.10 p.u.
r_f	Filter inductance	0.0005 p.u.
c_f	Filter inductance	0.08 p.u.
$c_{dc,0}$	DC capacitor on bus #0	80000 μ F
$c_{dc,1}$	DC capacitor on bus #1	10000 μ F
c_{sc}	Supercapacitor (SC)	20000 F
c_{bc}	Boost converter's capacitor	5000 μ F
l_{bc}	Boost converter's inductor	0.4 mH
r_{bc}	Boost converter's resistor	1 m Ω
r_l	DC cable resistor	1 m Ω
l_l	AC cable inductor	0.6 mH
p_{sc}^*	SC setpoint	0.0 p.u.
p_{bess}^*	BESS setpoint	0.0 p.u.
p_{pv}^*	PV setpoint	0.5 p.u.
$p_{dc,load}$	Constant-power load on bus # 0	0.1 p.u.
q^*	Inverter reactive power setpoint	0.0 p.u.
v^*	Inverter voltage setpoint	1.05 p.u.
\underline{z}_v	Virtual impedance	$j0.1$ p.u.
I_{lim}	Current limit	1.2 p.u.
r_f	Fault resistance at bus 680	0.01 Ω
Δp_{load}	Load disturbance at bus 680	5 MW
f_{sw}	Switching frequency	5 kHz
T_s	Simulation step size	5 μ s

The DER aggregation comprises an SC, a BESS, and a PV system (*power-reserved sufficiently with a higher voltage than the maximum power point* [53]), with power setpoints as 0.0, 0.0, and 0.5 p.u., respectively. To disaggregate the desired power response, $T_{des}^{vdcf-1} T_{des}^{fp-1}$, we pre-specify the SC's response as $T_{sc} := -\tau_{sc}s, \tau_{sc} \geq 0$ [one can alternatively assign a high-pass filter $m_i(s)$ for it as in (3-5)], considering its fast-acting capability to contribute an inertial response. Then, the desired collective response of the BESS and PV is represented as $T_{bess\&pv} := T_{des}^{vdcf-1} T_{des}^{fp-1} - T_{sc} + 1/2 (c_{dc,0} + 3c_{bc})s$ using the aggregation condition in (3-4), where $1/2 (c_{dc,0} + 3c_{bc})s$ denotes the non-controllable DC capacitors' response. Lastly, $T_{bess\&pv}$ is disaggregated between the BESS and the PV using dynamic participation factors. We choose a low-pass filter $m_{pv}(s) = \eta_{pv}/0.5s + 1$ for the power-reserved PV to provide power support relatively slowly while for a longer time. The residual part $m_{bess}(s) = 0.5s + 1 - \eta_{pv}/0.5s + 1$ is assigned to the BESS. Their desired power responses are represented by $T_{pv} = m_{pv}(s)T_{bess\&pv}$ and $T_{bess} = m_{bess}(s)T_{bess\&pv}$.

4.2.2 Case Study A: Connection to an Infinite-Bus System

- Case Study A1: Grid Disturbances

This study aims to validate the dynamic response of the basic grid interface in Figure 4-13(a) under grid frequency and voltage dips. We test both control implementations shown in Figure 3-2 for the DC-DC converters: I. DC grid-supporting and II. DC grid-forming. For the former, we choose $T_{sc} = -\frac{0.2s}{0.01s+1}$, $T_{pv} = 0.7/0.5s + 1 T_{bess\&pv}$, $T_{bess} = 0.5s + 0.3/0.5s + 1 T_{bess\&pv} \frac{1}{(0.01s+1)^2}$ (all in per-unit), where T_{sc} and T_{bess} are causalized by low-pass filters with a small time constant 0.01. For the latter, we specify $T_{sc}^{-1} = -\frac{1}{0.2s}$, $T_{pv}^{-1} = 0.5s + 1/0.7 T_{bess\&pv}^{-1} \frac{1}{0.01s+1}$, and $T_{bess}^{-1} = \frac{1}{T_{bess\&pv} - T_{pv}}$. The Bode diagrams of these transfer functions are shown in Figure 4-14, and the simulation results in Figure 4-15. It can be seen that the grid interface behaves according to the desired response. More specifically, the DC voltage and AC frequency responses well-match the re-aggregated desired responses using causalized T_i or T_i^{-1} , i.e., $T_{des}^{vdcf-1}(\sum_i T_i)^{-1}$, both in Figure 4-15(a) and (b). This suggests that all local converter controls satisfactorily achieve their desired control behaviours.

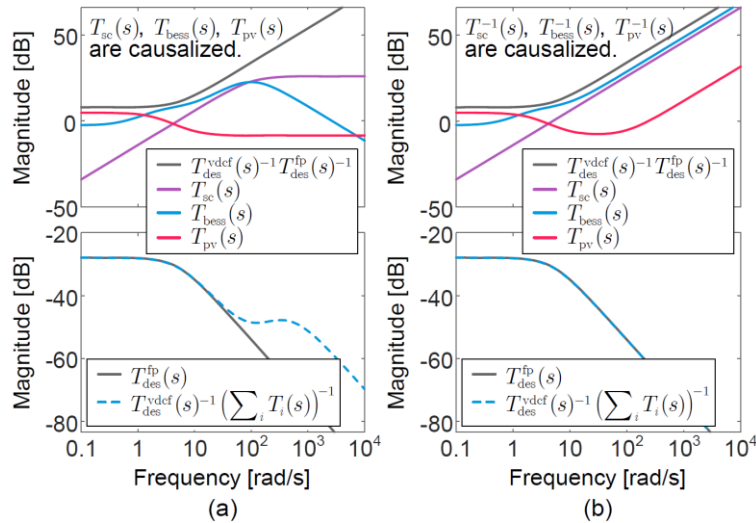


Figure 4-14 – Magnitude Bode plots, where $T_{des}^{vdcf-1} T_{des}^{fp-1}$ denotes the desired power response; T_{sc} , T_{bess} , and T_{pv} the power responses of the DERs; T_{des}^{fp} the desired frequency response; and $T_{des}^{vdcf-1} (\sum_i T_i)^{-1}$ the desired frequency response using causalized T_i or T_i^{-1} . (a) For the DC grid-supporting implementation. (b) For the DC grid-forming implementation.

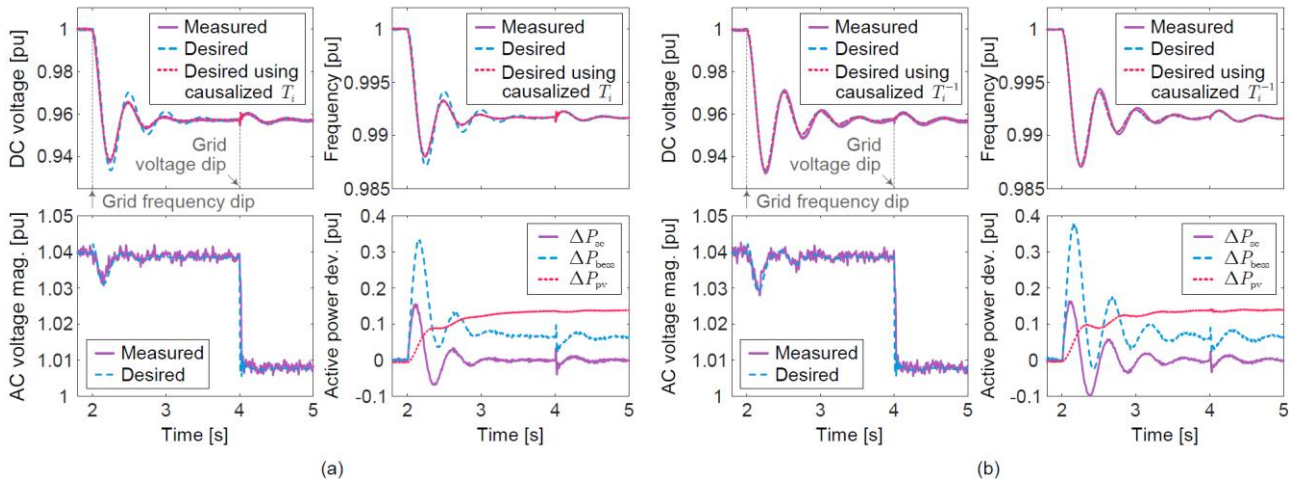


Figure 4-15 – Simulation results of case study A1: the basic grid interface in Figure 4-13(a) under a grid

frequency dip and a voltage dip. The control of the DC-DC converters uses (a) DC grid-supporting implementation and (b) DC grid-forming implementation. The ripples in the waveforms are due to the IGBT switching.

In Figure 4-15(a), where the DC grid-supporting implementation is used, the measured response slightly deviates from (more precisely, better than) the original desired response. This deviation is due to the effect of the low-pass filters that are used to causalize T_i . In particular, the low-pass filters in T_i produce a lead compensation in the re-aggregated frequency dynamics $T_{des}^{vdcf-1}(\sum_i T_i)^{-1}$, as indicated by the Bode diagram in Figure 4-14(a), introducing a dynamic damping effect and improving the dynamic performance. This implies that the basic inertial and droop response is not necessarily optimal and that we should have included a power oscillation damping service in the desired specification; see [35] for a systematic approach for choosing an optimal T_{des}^{fp} . Given this better damping (and easier power limiting), the DC grid-supporting implementation is recommended and used in the subsequent case studies.

- Case Study A2: Different Coordination Between DERs

This case study aims to test the robustness of the control design under different disaggregation settings. First, we specify different time constants for the SC's inertial response: $T_{sc} = -\frac{\tau_{sc}s}{0.01s+1}$, $\tau_{sc} \in \{0.0, 0.1, 0.2, 0.3, 0.4\}$. Then, $T_{bess\&pv}$ is disaggregated as in case study A1 such that the collective power response remains unchanged. The simulation results are shown in Figure 4-16(a), where the SC contributes different amounts of inertial power depending on the time constant. When the SC contributes less inertial power, the BESS delivers more inertial power. Moreover, we enable power limitations of 0.3, 0.3, and 0.7 p.u. in this case study for the SC, the BESS, and the PV, respectively. For small $\tau_{sc} \in \{0, 0.1, 0.2\}$ assigned to the SC, the power response of the BESS reaches the power limit. As a result, the frequency response cannot well-match the desired, showing a faster RoCoF. This suggests that the coordination of DERs should consider not only their dynamic characteristics but also their static capabilities/limitations. In Figure 4-16(b), we fix $T_{sc} = -\frac{0.3s}{0.01s+1}$ while specifying different static gains for the PV's participation factor: $T_{pv} = \eta_{pv}/0.5s + 1$, $T_{bess\&pv} = \frac{1}{(0.01s+1)^2}$, $\eta_{pv} \in \{0.6, 0.7, 0.8, 0.9, 1.0\}$. Figure 4-16 shows that PV provides increasing static power as the static gain grows. The collective responses comply with the desired since the power limitations are not triggered.

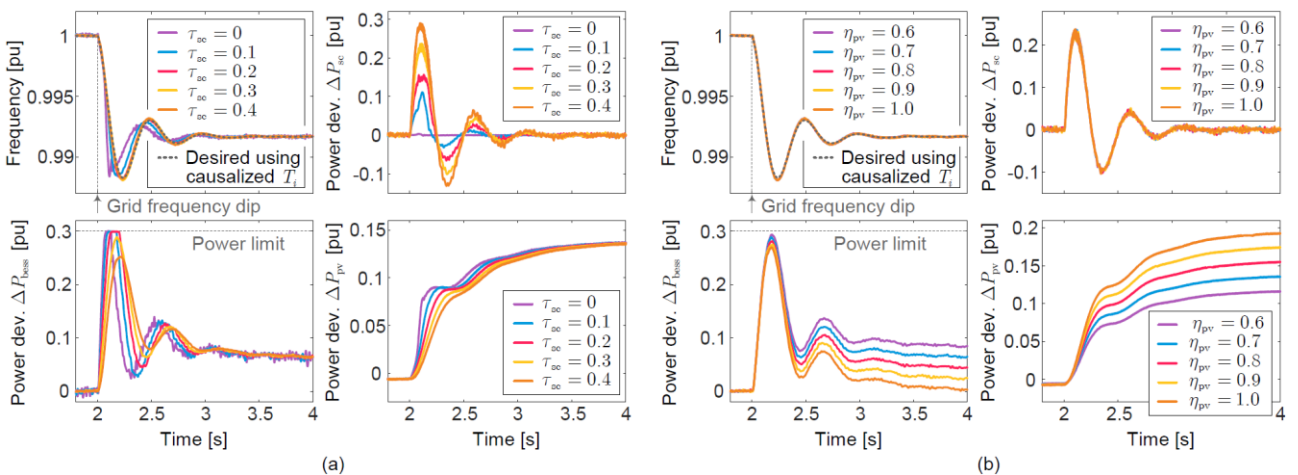


Figure 4-16 – Simulation results of case study A2: the basic grid interface in Figure 4-13(a) with different coordination between the DERs. (a) Different inertia time constants τ_{sc} in the SC's power response $T_{sc} =$

$-\frac{\tau_{sc}s}{0.01s+1}$. (b) Different participation factor static gains η_{pv} in the PV's power response $T_{pv} = \eta_{pv}/0.5s + 1 T_{bess\&pv}$.

- Case Study A3: Multi-DC-Bus Grid Interface Performance

This case study tests the performance of a multi-DC-bus grid interface. The original PV is replaced with two small PVs (with 70% and 30% of the original PV capacity, respectively), as shown in Figure 4-13(b), and we choose T_{sc} , T_{pv} , and T_{bess} the same as case study A1, whereas $T_{des}^{vdcvdc} = 1$, $T_{pv1} = 0.7 \times T_{pv}$, and $T_{pv2} = 0.3 \times T_{pv}$, all in per-unit. In the DC-coupled DC-output module, T_{pv} , T_{pv1} , and T_{pv2} control the central, PV1's, and PV2' DC-DC converters, respectively. The simulation results are shown in Figure 4-17. We can see that the response of the entire interface matches the desired response, where the two PVs contribute in proportion 7:3, as designed. Since the sub-interface delivers a little more power to compensate for power losses, DC bus #1's voltage is lower than DC bus #0's voltage in the post-disturbance steady state.

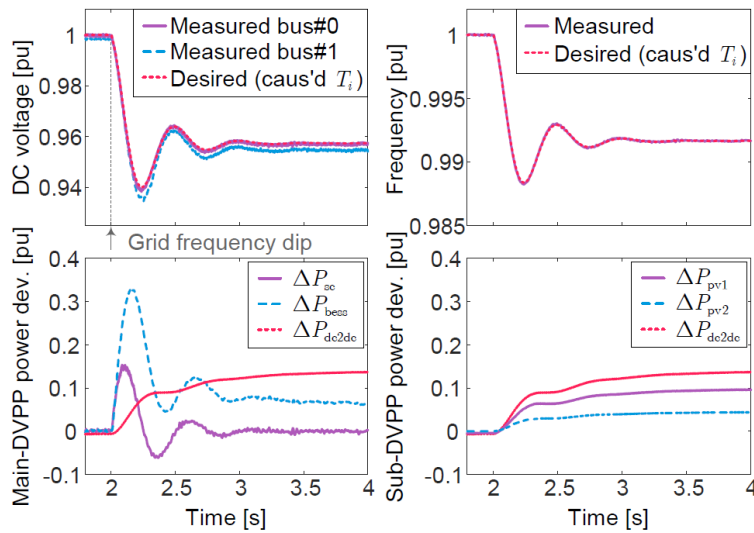


Figure 4-17 – Simulation results of case study A3: the multi-DC-bus grid interface in Figure 4-13(b) under a grid frequency dip.

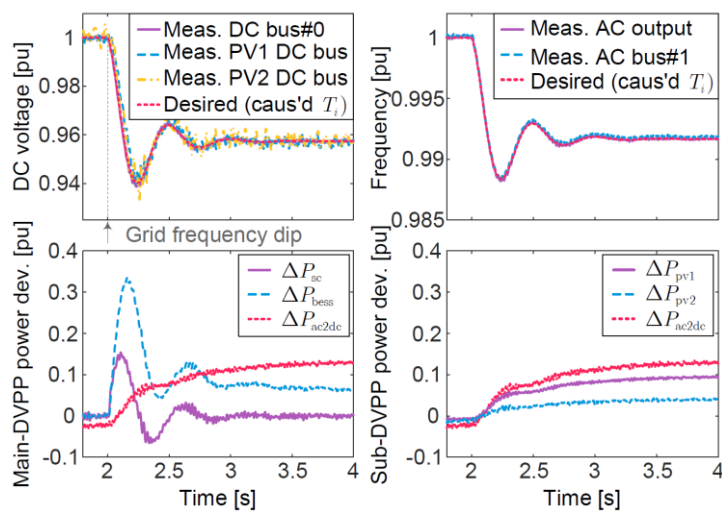


Figure 4-18 – Simulation results of case study A4: the AC/DC hybrid grid interface in Figure 4-13(c) under a grid frequency dip.

- Case Study A4: AC/DC Hybrid Grid Interface Performance

This case study tests the performance of a modular AC/DC hybrid grid interface. Instead of the DC-

coupled DC-output module in case study A3, this case study introduces an AC-coupled DC-output module, with two small PVs, as illustrated in Figure 4-13(c). Thus, this system can represent a grid-connected AC/DC hybrid microgrid. The PV capacities and the disaggregation of the desired response are similar to case study A3. More specifically, $T_{pv1} = 0.7 \times T_{pv}$ and $T_{pv2} = 0.3 \times T_{pv}$ are used to control two PVs' DC-DC converters, respectively. Moreover, both the PVs' DC-AC inverters and the central AC-DC rectifier use T_{des}^{vdcf-1} for AC-DC matching frequency-forming control and T_{des}^{vq} for voltage-forming control. The simulation results are shown in Figure 4-18. It can be seen that the response of the entire interface satisfies the desired response, where the two PVs contribute power support in proportion 7:3, as designed. Furthermore, due to the AC-DC matching relationship across the inverters and the rectifier, DC bus #0 and the DC buses of both PVs' inverters share (almost) the same DC voltage response, and also AC bus #1 and the output-terminal AC bus share (almost) the same frequency response.

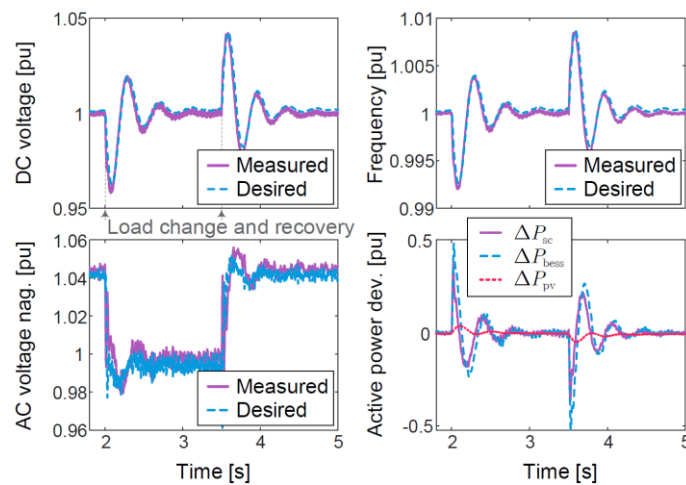


Figure 4-19 – Simulation results of case study B1: the grid interface connected to the IEEE 13-bus system in Figure 4-13(d) under load change and recovery.

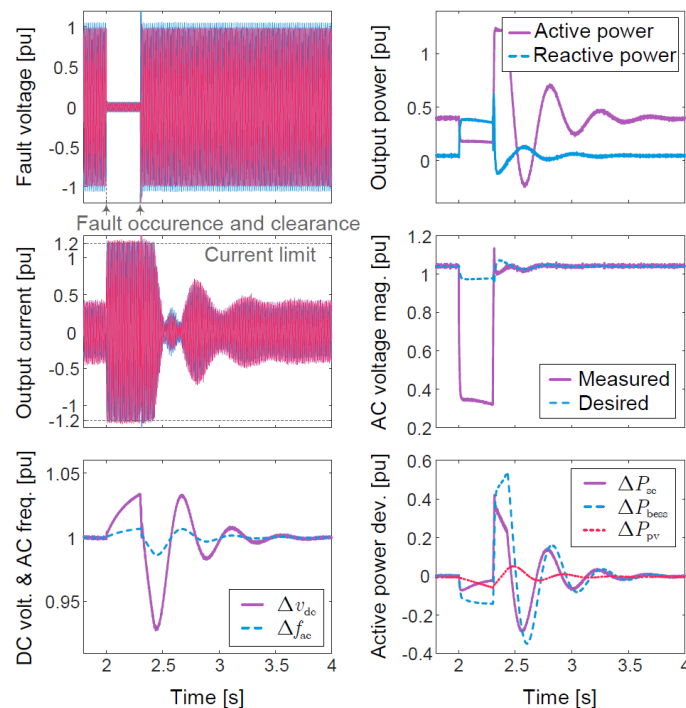


Figure 4-20 – Simulation results of case study B2: the grid interface connected to the IEEE 13-bus system in



Figure 4-13(d) under a grid short-circuit fault.

4.2.3 Case Study B: Connection to the IEEE 13-Bus System

- Case Study B1: Load Disturbance

This case study aims to validate the grid interface performance in a more realistic grid context. As shown in Figure 4-13(d), a basic grid interface is connected through a transmission line to bus 680 of the IEEE 13-bus distribution system [58]. A load disturbance of 5 MW is imposed on bus 680. In the simulation result of Figure 4-19, the load disturbance occurs at 2 s and disappears at 3.5 s. We can see that the measured response to the disturbance matches the desired response well in terms of the DC voltage, the AC frequency, and the AC voltage magnitude. Moreover, since the frequency recovers to the nominal due to the presence of the main grid (modelled in an infinite bus), the grid interface only contributes an inertial response in terms of active power. Accordingly, the main contributors are the SC and the BESS.

- Case Study B2: Short-Circuit Fault

This case study tests the fault ride-through performance of the grid interface in Figure 4-13(d). A short-circuit fault is imposed on bus 680 for a duration of 0.3 s. To limit the fault current, the current limiter in the inverter control (as illustrated in Figure 3-2) is enabled, and an additional feedback loop of current saturation information is activated during the current saturation [54]. This is to maintain the grid-forming frequency/angle control while enforcing the current magnitude limiting for fault ride-through; see our recent work [54] for further details on fault current limiting. The response of the grid interface under the grid fault is shown in Figure 4-20. The current magnitude is limited at a pre-specified level of 1.2 p.u., and consequently, the AC voltage response deviates largely from the nominally desired response. The reactive power increases to respond to the voltage dip. Moreover, since the AC GFM and AC-DC matching functionalities are maintained during the grid fault [54], the DC voltage and the AC frequency are still under regulation even in the case of current saturation. Therefore, the DERs reduce their power outputs by utilizing the droop regulation characteristics when the DC voltage rises. After grid fault recovery and the current exits from saturation, the grid interface recovers to normal operation, matching the nominally desired response. The results of this case study validate the resilience of the proposed grid interface control under grid faults and demonstrate its compatibility with existing inner control and protection loops.

5 Conclusion

We have presented a systematic approach to provide optimal dynamic ancillary services with converter-interfaced systems (e.g., AGIs) based on local power grid perception. To do so, we used the “*perceive-and-optimize*” (P&O) strategy. We first identified a grid dynamic equivalent at the interconnection terminals of the converter, and then established a closed-loop system interconnection of the identified grid equivalent and a desired transfer function matrix, where we optimize for the latter to provide optimal dynamic ancillary services. In the process, we ensure that grid-code and device-level requirements are satisfied. Our numerical experiments verify the superiority of our approach over cheap ancillary services provision based on minimum (open-loop) grid-code requirements, especially during changing grid-conditions.

We further present a generic, flexible, and modular AGI design to achieve the aggregate GFM dynamic ancillary services of heterogeneous DERs. Particularly, for a DC-coupled AC-output grid interface, the proposed control design allows for a desired AC GFM response, AC-DC matching behaviour, and coordinated power contribution between heterogeneous DERs. Based on the four basic AGIs, we develop and comprehensively validate a systematic top-down approach for assembling and controlling modular AGIs and more generally modular AC/DC hybrid power grids.

The provision of the proposed “high-performing dynamic ancillary services” computed via the P&O strategy is primarily relevant for system operators, as it allows for improved performance of the overall power grid behaviour. In this regard, an immediate use case of our approach could be the implementation in STATCOMs or HVDC stations, as they are typically owned by the system operator. However, also from the viewpoint of external generating units not owned by the system operator, the P&O strategy offers several *local benefits*, such as improved small-signal stability, equipment protection, increased power quality, damping of local oscillations, etc. Nevertheless, despite these advantages, the current common practice typically considers it to be more convenient and profitable to just take cheap and minimal efforts to satisfy (open-loop) grid-code requirements, albeit being less performant and even prone to failure under particular grid conditions. As this approach will no longer ensure reliable future power system operation, it is essential to encourage the implementation of high-performing dynamic ancillary services by external generating units.

In terms of AGI control, there are several critical directions for further research. One is to explore top-down paradigms to design, shape, and manage the dynamic behaviour of AC/DC hybrid power grids, in contrast to traditional bottom-up paradigms that rely on modelling, analysis, and design from device-level individual components to the grid-level whole system. Another direction is the development of standardized protocols or new-generation grid codes to promote the widespread adoption and interoperability of such top-down design paradigms.

A. Appendix A Dynamic Ancillary Services as Transfer Functions

This appendix shows the translated parametric transfer functions as well as the ancillary service constraints imposed by grid-code and device-level requirements.

A.1 Translated Parametric Transfer Functions

The rational parametric transfer functions $T_{des}^{fcr}(s, \alpha^{fcr})$, $T_{des}^{ffr}(s, \alpha^{ffr})$ and $T_{des}^{vq}(s, \alpha^{vq})$ in Section 1.1.1 are obtained by translating the associated piece-wise linear time-domain grid-code curves in Figure 1-1 and Figure 1-2(b) into the frequency domain. This can be achieved by applying our recent method in [34], which is based on piece-wise affine time-domain parametrizations and Laplace transformations, followed by Padé approximations of appropriate order n . In particular, the resulting parametric transfer function expressions as a function of the parameters α turn out to be quite intricate, i.e.,

$$\begin{aligned}
 T_{des}^{fcr}(s, \alpha^{fcr}) &= 1/D_p/s(t_a^{fcr} - t_i^{fcr}) \left((1 - t_i^{fcr}/2ns)^n / (1 + t_i^{fcr}/2ns)^n - (1 - t_a^{fcr}/2ns)^n / (1 + t_a^{fcr}/2ns)^n \right) \\
 T_{des}^{ffr}(s, \alpha^{ffr}) &= 1/K_p/s t_a^{ffr} \left(1 - (1 - t_p^{ffr}/2ns)^n / (1 + t_p^{ffr}/2ns)^n \right) \\
 &\quad + 1/K_p(1 - x^{ffr})/s(t_d^{ffr} - t_r^{ffr}) \left((1 - t_p^{ffr}/2ns)^n / (1 + t_p^{ffr}/2ns)^n - (1 - t_d^{ffr}/2ns)^n / (1 + t_d^{ffr}/2ns)^n \right) \\
 &\quad - 1/K_p/s(t_r^{ffr} - t_d^{ffr}) \left((1 - t_d^{ffr}/2ns)^n / (1 + t_d^{ffr}/2ns)^n - (1 - t_r^{ffr}/2ns)^n / (1 + t_r^{ffr}/2ns)^n \right) \\
 T_{des}^{vq}(s, \alpha^{vq}) &= 0.9/D_q/t_{90}s \left(1 - (1 - t_{90}/2ns)^n / (1 + t_{90}/2ns)^n \right) \\
 &\quad + 0.1/D_q/(t_{100} - t_{90})s \left((1 - t_{90}/2ns)^n / (1 + t_{90}/2ns)^n - (1 - t_{100}/2ns)^n / (1 + t_{100}/2ns)^n \right),
 \end{aligned} \tag{A-1}$$

where $t_p^{ffr} = x^{ffr} t_a^{ffr}$.

A.2 Ancillary Services Constraints

The ancillary services constraints involve: FFR provision, auxiliary control provision, superimposed frequency control, and voltage control.

- FFR Provision

The constraint set which defines the grid-code and device-level requirements in (1-6) of the active power capability curve for FFR provision in Figure 1-1(b) is given as

$$\begin{aligned}
 0 \leq t_a^{ffr} &\leq t_{a,max}^{ffr} \\
 t_{d,min}^{ffr} &\leq t_d^{ffr} \\
 t_{r,min}^{ffr} &\leq t_r^{ffr} \\
 1 \leq x^{ffr} &\leq x_{max}^{ffr} \\
 |\Delta p_{ffr}^{max}| &\leq t_a^{ffr} \cdot r_{max}^p \\
 t_d^{ffr} &\leq t_{d,max}^{ffr} \\
 t_r^{ffr} &\leq t_{r,max}^{ffr} \\
 x^{ffr} &\leq m_{max}^p / |\Delta p_{ffr}^{max}|,
 \end{aligned} \tag{A-2}$$

where $t_{a,max}^{ffr}$ is the maximum admissible full activation time for the FFR provision. The FFR support duration time t_d^{ffr} is lower and upper bounded by the minimum and maximum support duration

$t_{d,\min}^{\text{ffr}}$ and $t_{d,\max}^{\text{ffr}}$, respectively⁶. Likewise, the minimum and maximum FFR return-to-recovery times are given by $t_{r,\min}^{\text{ffr}}$ and $t_{r,\max}^{\text{ffr}}$, respectively⁷. The FFR overdelivery factor x^{ffr} must not exceed $m_{\max}^p/|\Delta p_{\text{ffr}}^{\text{max}}|$, where m_{\max}^p is the reserve unit's maximum active power peak capacity, and $|\Delta p_{\text{ffr}}^{\text{max}}| = |1/K_p \Delta f_{\max}|$ is the maximum FFR capacity. Additionally, x^{ffr} has to be smaller than the maximum tolerable overdelivery factor $x_{\max}^{\text{ffr}} \in [1,2]$ specified in the grid code. As for the FCR constraints in (1-4) in the revised manuscript, r_{\max}^p is the maximal active power ramping rate of the reserve unit. Finally, the grid-code and device-level specification sets as in (1-6) are defined as $\mathcal{G}^{\text{ffr}} = \{t_a^{\text{ffr}}, t_d^{\text{ffr}}, t_r^{\text{ffr}}, x^{\text{ffr}} \mid (A-2)\}$ and $\mathcal{D}^{\text{ffr}} = \{t_a^{\text{ffr}}, t_d^{\text{ffr}}, t_r^{\text{ffr}}, x^{\text{ffr}} \mid (A-2)\}$, respectively, and all constraint parameters are further specified in Table 1-1.

- Auxiliary Control Provision

The constraint set which defines the grid-code and device-level requirements in (1-8) of the bandpass resonator transfer function in Figure 1-2(a) for auxiliary control provision (e.g., POD) is given as

$$\begin{aligned}
 \omega_{\min} &\leq \omega_l \\
 \omega_h &\leq \omega_{\max} \\
 \omega_l &\leq \omega_h \\
 |\Delta p_{\text{aux}}^{\text{peak,max}}(\alpha^{\text{aux}})| &\leq m_{\max}^p \\
 0 \leq t_{\text{aux}}^s(\alpha^{\text{aux}}) &\leq t_{a,\max}^{\text{ffr}} \\
 0 \leq t_{\text{aux}}^s(\alpha^{\text{aux}}) &\leq t_{i,\max}^{\text{fcr}},
 \end{aligned} \tag{A-3}$$

where ω_{\min} and ω_{\max} are the lower and upper bounds of the bandpass frequency range. Again, m_{\max}^p is the reserve unit's maximum active power peak capacity, and $|\Delta p_{\text{aux}}^{\text{peak,max}}(\alpha^{\text{aux}})|$ is the parametric time-domain expression of the maximum peak power injection after a step disturbance, which can be obtained from the time-domain expression of $T_{\text{des}}^{\text{aux}}(s, \alpha^{\text{aux}})$ as

$$|\Delta p_{\text{aux}}^{\text{peak,max}}(\alpha^{\text{aux}})| = \left| 2m_{\text{aux}} / \sqrt{\omega_d^2 + 1} e^{-\arctan(\omega_d)/\omega_d} \cdot \Delta f_{\max} \right|, \tag{A-4}$$

where $\omega_d = \sqrt{4\omega_l\omega_h/(\omega_h - \omega_l)^2 - 1} \in \mathbb{R}$. Moreover, the constraints in the last two sub-equations in (A-3) ensure that the time-domain pulse width $t_{\text{aux}}^s(\alpha^{\text{aux}}) = 9.2/\omega_h - \omega_l$ of the auxiliary active power injection is not interfering with the minimum grid-code requirements of the FCR and FFR injection.

Finally, the grid-code and device-level specification sets of the auxiliary control provision as in (1-8) are defined as $\mathcal{G}^{\text{aux}} = \{\omega_l, \omega_h, m_{\text{aux}} \mid (A-3)\}$ and $\mathcal{D}^{\text{aux}} = \{\omega_l, \omega_h, m_{\text{aux}} \mid (A-3)\}$, respectively, and all constraint parameters are further specified in Table 1-1.

- Superimposed Frequency Control

By superimposing the FCR, FFR and auxiliary control transfer functions, we can establish the overall frequency control specification $T_{\text{des}}^{\text{fp}}(s, \alpha^{\text{fp}})$ as in (1-3). While doing so, we further need to

⁶ In our work, we assume $t_{d,\min}^{\text{ffr}} \gg t_{a,\max}^{\text{ffr}} + t_a^{\text{ffr}}$, which is typically the case in today's grid codes.

⁷ In our work, we assume $t_{r,\min}^{\text{ffr}} \geq t_{a,\max}^{\text{ffr}} + t_d^{\text{ffr}}$, which is typically the case in today's grid codes.

ensure that the maximum capacity and bandwidth limitations of the reserve unit are not violated during such a superimposed injection of active power. This requires additional overall device-level constraints for the f-p control, which we approximate as

$$\begin{aligned}
 |\Delta p_{\text{fcr}}^{\text{max}}| + |x^{\text{ffr}} \Delta p_{\text{ffr}}^{\text{max}}| + |\Delta p_{\text{aux}}^{\text{peak,max}}(\alpha^{\text{aux}})| &\leq m_{\text{max}}^{\text{p}} \\
 |\Delta p_{\text{fcr}}^{\text{max}}| / (t_{\text{a}}^{\text{fcr}} - t_{\text{i}}^{\text{fcr}}) + |\Delta p_{\text{ffr}}^{\text{max}}| / t_{\text{a}}^{\text{ffr}} + |\Delta p_{\text{aux}}^{\text{peak,max}}(\alpha^{\text{aux}})| / t_{\text{aux}}^{\text{peak}}(\alpha^{\text{aux}}) &\leq r_{\text{max}}^{\text{p}},
 \end{aligned} \tag{A-5}$$

where $|\Delta p_{\text{fcr}}^{\text{max}}| = |1/D_{\text{p}} \Delta f_{\text{max}}|$ is the maximum FCR capacity, $|\Delta p_{\text{ffr}}^{\text{max}}| = |1/K_{\text{p}} \Delta f_{\text{max}}|$ the maximum FFR capacity, $t_{\text{aux}}^{\text{peak}}(\alpha^{\text{aux}}) = \arctan(\omega_{\text{d}}) / \zeta \omega_{\text{d}}$ the peak power injection time of $T_{\text{des}}^{\text{aux}}(s, \alpha^{\text{aux}})$ after a step disturbance with $\zeta = (\omega_{\text{h}} - \omega_{\text{l}}) / 2$, and $|\Delta p_{\text{aux}}^{\text{peak,max}}(\alpha^{\text{aux}})|$ the maximum peak power injection of $T_{\text{des}}^{\text{aux}}(s, \alpha^{\text{aux}})$ after a step disturbance as in (A-4). In particular, we encode these overall f-p device-level constraints in (A-5) via an additional constraint set $\mathcal{D}^{\text{fp}} = \{\alpha^{\text{fcr}}, \alpha^{\text{ffr}}, \alpha^{\text{aux}} \mid (\text{A-5})\}$.

- Voltage Regulation

The constraint set which defines the grid-code and device-level requirements in (1-9) of the reactive power capability curve in Figure 1-2(b) is given as

$$\begin{aligned}
 0 \leq t_{90}^{\text{vq}} &\leq t_{90,\text{max}}^{\text{vq}} \\
 t_{90}^{\text{vq}} \leq t_{100}^{\text{vq}} &\leq t_{100,\text{max}}^{\text{vq}} \\
 |\Delta q_{90}^{\text{max}}| &\leq t_{90}^{\text{vq}} \cdot r_{\text{max}}^{\text{q}} \\
 0.1 \cdot |\Delta q_{100}^{\text{max}}| &\leq (t_{100}^{\text{vq}} - t_{90}^{\text{vq}}) \cdot r_{\text{max}}^{\text{q}}
 \end{aligned} \tag{A-6}$$

where $t_{90,\text{max}}^{\text{vq}}$ and $t_{100,\text{max}}^{\text{vq}}$ are the maximum admissible activation times for the 90% and 100% reactive power capacity provision, respectively, $|\Delta q_{90}^{\text{max}}| = 0.9 \cdot |\Delta q_{100}^{\text{max}}|$ and $|\Delta q_{100}^{\text{max}}|$ are the maximum 90% and 100% reactive power capacity levels, and $r_{\text{max}}^{\text{q}}$ is the maximum reactive power ramping rate of the reserve unit. Finally, the grid-code and device-level specification sets as in (1-9) are defined as $\mathcal{G}^{\text{vq}} = \{t_{90}^{\text{vq}}, t_{100}^{\text{vq}} \mid (\text{A-6})\}$ and $\mathcal{D}^{\text{vq}} = \{t_{90}^{\text{vq}}, t_{100}^{\text{vq}} \mid (\text{A-6})\}$, respectively, and all constraint parameters are further specified in Table 1-1.

B. Appendix B H2 Optimization Problem

The \mathcal{H}_2 -norm between the disturbance input w and the performance output \tilde{z}_p of the system in (2-9) is given by [51]

$$\begin{aligned} J &= \|\tilde{T}_{cl}(s, \alpha)\|_2^2 \\ &= \text{trace}(C_{cl}(\alpha)PC_{cl}(\alpha)^\top) \\ &= \text{trace}(B_{cl}(\alpha)^\top QB_{cl}(\alpha)), \end{aligned} \quad (\text{B-1})$$

where P and Q are the observability and controllability Gramian obtained as the positive definite solutions of the Lyapunov equation and its dual

$$\begin{aligned} A_{cl}(\alpha)P + PA_{cl}(\alpha)^\top + B_{cl}(\alpha)B_{cl}(\alpha)^\top &= \mathbb{O} \\ A_{cl}(\alpha)^\top Q + QA_{cl}(\alpha) + C_{cl}(\alpha)^\top C_{cl}(\alpha) &= \mathbb{O}, \end{aligned} \quad (\text{B-2})$$

parameterized in α for the given closed-loop system matrices $A_{cl}(\alpha)$, $B_{cl}(\alpha)$ and $C_{cl}(\alpha)$. Based on the latter, the optimization problem in (2-11) to compute the locally optimal α^* with respect to the \mathcal{H}_2 norm $\|\tilde{T}_{cl}(s, \alpha)\|_2^2$ can be reformulated as

$$\begin{aligned} \underset{\alpha, P, Q}{\text{minimize}} \quad & \text{trace}(C_{cl}(\alpha)PC_{cl}(\alpha)^\top) \\ \text{subject to} \quad & \alpha \in \mathcal{G} \cap \mathcal{D}, \text{ (B-2)}, P > 0, Q > 0. \end{aligned} \quad (\text{B-3})$$

The constraints (B-2) make the problem (B-3) non-convex and difficult to solve. However, since the objective function is smooth, an explicit gradient $\nabla_\alpha J = \nabla_\alpha \text{trace}(C_{cl}(\alpha)PC_{cl}(\alpha)^\top)$ can be derived and directly used to solve (B-3) for the (locally) optimal parameter vector α^* via scalable first-order methods such as projected gradient descent, i.e.,

$$\alpha^{k+1} = \text{proj}_{\mathcal{G} \cap \mathcal{D}}[\alpha^k - \gamma^k \text{grad}J(\alpha^k)], \quad (\text{B-4})$$

where $\gamma^k \in \mathbb{R}$ is the step-size parameter, and $\text{proj}_{\mathcal{G} \cap \mathcal{D}}[\cdot]$ the projection operator which is defined as

$$\begin{aligned} \text{proj}_{\mathcal{G} \cap \mathcal{D}}[\xi] &= \underset{y \in \mathbb{R}^n}{\text{argmin}} \quad 1/2 \|y - \xi\|_2^2 \\ \text{s.t.} \quad & y \in \mathcal{G} \cap \mathcal{D}. \end{aligned} \quad (\text{B-5})$$

The term $\text{grad}J(\alpha^k)$ specifies a gradient direction which allows for several implementation options or variants thereof, e.g.,

- $\text{grad}J(\alpha^k) = \nabla_\alpha J(\alpha^k)$ for classical gradient descent methods [59], or
- $\text{grad}J(\alpha^k) = \text{sgn}(\nabla_\alpha J(\alpha^k))$ for sign gradient descent methods [60][61][62],

In particular, sign gradient descent methods represent a widely adopted metaheuristic approach known for their typically faster convergence properties and increased likelihood of finding the global optimum compared to classical gradient descent methods. Moreover, they demonstrate reduced sensitivity to step size and initial conditions (further details can be found in [60][61][62]). In any case, for all the above implementation options, by using steps similar to the ones in [8], the gradient with respect to α can be computed as

$$\nabla_\alpha J = [\partial J / \partial \alpha_1, \partial J / \partial \alpha_2, \dots, \partial J / \partial \alpha_n]^\top, \quad (\text{B-6})$$

where each component $\partial J / \partial \alpha_i$ is given as

$$\partial J / \partial \alpha_i = 2 \cdot \text{trace}(\partial A_{cl} / \partial \alpha_i PQ) + \text{trace}(\partial (B_{cl} B_{cl}^\top) / \partial \alpha_i Q) + \text{trace}(P \partial (C_{cl}^\top C_{cl}) / \partial \alpha_i). \quad (\text{B-7})$$

C. Appendix C Control Objectives and Designs for Basic AGIs

This appendix shows the control objectives and designs of the other three basic grid interfaces that are not detailed in the main text. The aggregation conditions are focused, as the disaggregation and implementation are similar to the previous DC-coupled AC-output module.

C.1 AC-Coupled DC-Output Grid Interface

We specify the desired power response Δp of the central rectifier to an output-terminal DC voltage variation $\Delta(v_{dc}^2)$ as

$$\Delta p(s) = T_{des}^{pvdc}(s)\Delta(v_{dc}^2)(s). \quad (C-1)$$

Similar to (1-12), we specify a desired AC-DC matching relationship across the rectifier as

$$\Delta(v_{dc}^2)(s) = T_{des}^{vdcf}(s)\Delta f(s), \quad (C-2)$$

where Δf denotes the frequency variation of the AC-coupling bus. Moreover, the frequency response of each inverter connecting the DER is specified as

$$\Delta f_i(s) = T_i(s)\Delta p_i(s), \quad (C-3)$$

with the frequency-forming variable Δf_i and the measured power change Δp_i . Based on this, the coherent frequency at the AC-coupling bus can be derived as

$$\Delta f_{sync}(s) = \left(\sum_i T_i(s)^{-1} \right)^{-1} \sum_i \Delta p_i(s). \quad (C-4)$$

From (C-1), (C-2), (C-4), the frequency coherency $\Delta f \approx \Delta f_{sync}$, and the power conservation $\Delta p = \sum_i \Delta p_i$, the aggregation condition for the AC-coupled DC-output grid interface is derived as

$$\sum_i T_i(s)^{-1} = T_{des}^{vdcf}(s)T_{des}^{pvdc}(s). \quad (C-5)$$

C.2 AC-Coupled AC-Output Grid Interface

Similar to (1-11) as for a DC-coupled AC output module, we specify the desired frequency response Δf as

$$\Delta f(s) = T_{des}^{fp}(s)\Delta p(s), \quad (C-6)$$

where Δp is the active power change at the output terminal. The frequency response of each inverter can be specified as in (C-3). We can immediately obtain the aggregation condition from the coherent frequency dynamics in (C-4) as

$$\left(\sum_i T_i(s)^{-1} \right)^{-1} = T_{des}^{fp}(s). \quad (C-7)$$

C.3 DC-Coupled DC-Output Grid Interface

We specify the desired power response Δp of the central DC-DC converter to an output-terminal DC voltage variation $\Delta(v_{dc}^2)$ as

$$\Delta p(s) = T_{des}^{pvdc}(s)\Delta(v_{dc}^2)(s). \quad (C-8)$$

Likewise, we desire a DC-DC matching relationship between the input voltage $\Delta(v_{dc,1}^2)$ and the output voltage $\Delta(v_{dc}^2)$ as

$$\Delta(v_{dc,1}^2)(s) = T_{des}^{vdcvdc}(s)\Delta(v_{dc}^2)(s). \quad (C-9)$$

Furthermore, as in (1-13), the power response of each DC-DC converter connecting the DER is represented as

$$\Delta p_i(s) = T_i(s)\Delta(v_{dc,1}^2)(s). \quad (C-10)$$

From (C-8) to (C-10) and the power conservation relationship $\Delta p = \sum_i \Delta p_i(s)$, the aggregation condition for a DC-coupled DC-output grid interface is derived as

$$\sum_i T_i(s) = T_{des}^{vdcvdc}(s)^{-1}T_{des}^{pvdc}(s). \quad (C-11)$$



References

- [1] E. Commission, "Commission regulation (EU) 2016/631 of 14 April 2016, establishing a network code on requirements for grid connection of generators," Off. J. Eur. Union, 2016.
- [2] F. Oyj, "The technical requirements and the prequalification process of fast frequency reserves (FFR)," 2021.
- [3] EirGrid, "DS3 system services agreement," 2018.
- [4] N. Modig, R. Eriksson, L. Haarla, P. Ruokolainen, M. Kuivaniemi, K. Hornnes, P. Vada, S. Meybodi, and D. Karlsson, "Technical requirements for fast frequency reserve provision in the nordic synchronous area," ENTSO-E, 2019.
- [5] H. Geng, X. Xi, and G. Yang, "Small-signal stability of power system integrated with ancillary-controlled large-scale DFIG-based wind farm," *IET Renewable Power Generation*, vol. 11, no. 8, pp. 1191–1198, 2017.
- [6] J. Ying, X. Yuan, J. Hu, and W. He, "Impact of inertia control of DFIG based wt on electromechanical oscillation damping of sg," *IEEE Trans. Power Syst.*, vol. 33, no. 3, pp. 3450–3459, 2018.
- [7] B. K. Poolla, D. Gros, and F. Dorfler, "Placement and implementation of grid-forming and grid-following virtual inertia and fast frequency response," *IEEE Trans. Power Syst.*, vol. 34, no. 4, pp. 3035–3046, 2019.
- [8] A. Ademola-Idowu and B. Zhang, "Optimal design of virtual inertia and damping coefficients for virtual synchronous machines," in *2018 IEEE Power & Energy Society General Meeting (PESGM)*, pp. 1–5.
- [9] D. Gros, S. Bolognani, B. K. Poolla, and F. Dorfler, "Increasing the resilience of low-inertia power systems by virtual inertia and damping," in *Proceedings of IREP'2017 Symposium. International Institute of Research and Education in Power System Dynamics*, 2017, p. 64.
- [10] L. Ruttledge and D. Flynn, "Emulated inertial response from wind turbines: gain scheduling and resource coordination," *IEEE Trans. Power Syst.*, vol. 31, no. 5, pp. 3747–3755, 2015.
- [11] Z. Wu, W. Gao, T. Gao, W. Yan, H. Zhang, S. Yan, and X. Wang, "State-of-the-art review on frequency response of wind power plants in power systems," *Journal of Modern Power Systems and Clean Energy*, vol. 6, no. 1, pp. 1–16, 2018.
- [12] K. Clark, N. W. Miller, and J. J. Sanchez-Gasca, "Modeling of GE wind turbine-generators for grid studies," *GE energy*, vol. 4, pp. 0885–8950, 2010.
- [13] C. Roberts, D. Arnold, and D. S. Callaway, "An online adaptive damping controller for converter-interfaced generation," *IEEE Trans. Power Syst.*, 2023.
- [14] T. S. Babu, K. R. Vasudevan, V. K. Ramachandaramurthy, S. B. Sani, S. Chemud, R. M. Lajim, A comprehensive review of hybrid energy storage systems: Converter topologies, control strategies and future prospects, *IEEE Access* 8 (2020) 148702–148721. doi:10.1109/ACCESS.2020.3015919.
- [15] A. Mohammed, S. S. Refaat, S. Bayhan, H. Abu-Rub, AC microgrid control and management strategies: Evaluation and review, *IEEE Power Electronics Magazine* 6 (2) (2019) 18–31. doi:10.1109/MPEL.2019.2910292.
- [16] A. Navarro-Rodriguez, P. Garcia, C. Gomez-Aleixandre, C. Blanco, Cooperative primary control of a hybrid AC/DC microgrid based on AC/DC virtual generators, *IEEE Transactions on Energy Conversion* 37 (4) (2022) 2837–2850. doi:10.1109/TEC.2022.3203770.
- [17] R. Rosso, X. Wang, M. Liserre, X. Lu, S. Engelken, Grid-forming converters: Control approaches, grid-synchronization, and future trends—a review, *IEEE Open Journal of Industry Applications* 2 (2021) 93–109. doi:10.1109/OJIA.2021.3074028.
- [18] H. Gao, H. Xin, L. Huang, Z. Li, W. Huang, C. Wu, P. Ju, Common-mode frequency in converter-integrated power systems: Definition, analysis, and quantitative evaluation, *IEEE Transactions on Power Systems* 37 (6) (2022) 4846–4860. doi:10.1109/TPWRS.2022.3150912.



- [19] V. Haberle, A. Tayyebi, X. He, E. Prieto-Araujo, F. Dorfler, Grid-forming and spatially distributed control design of dynamic virtual power plants, *IEEE Transactions on Smart Grid* 15 (2) (2024) 1761–1777. doi:10.1109/TSG.2023.3311481.
- [20] Y. Gu, W. Li, X. He, Frequency-coordinating virtual impedance for autonomous power management of DC microgrid, *IEEE Transactions on Power Electronics* 30 (4) (2015) 2328–2337. doi:10.1109/TPEL.2014.2325856.
- [21] C. A. Macana, E. Mojica-Nava, H. R. Pota, J. Guerrero, J. C. Vasquez, A distributed real-time energy management system for inverter-based microgrids, *Electric Power Systems Research* 213 (2022) 108753. doi:10.1016/j.epsr.2022.108753.
- [22] M. M. Mohamed, H. M. El Zoghby, S. M. Sharaf, M. A. Mosa, Optimal virtual synchronous generator control of battery/supercapacitor hybrid energy storage system for frequency response enhancement of photovoltaic/diesel microgrid, *Journal of Energy Storage* 51 (2022) 104317. doi:10.1016/j.est.2022.104317.
- [23] C. Sun, S. Q. Ali, G. Joos, F. Bouffard, Design of hybrid-storage-based virtual synchronous machine with energy recovery control considering energy consumed in inertial and damping support, *IEEE Transactions on Power Electronics* 37 (3) (2022) 2648–2666. doi:10.1109/TPEL.2021.3111482.
- [24] D. Chen, Y. Xu, A. Q. Huang, Integration of DC microgrids as virtual synchronous machines into the AC grid, *IEEE Transactions on Industrial Electronics* 64 (9) (2017) 7455–7466. doi:10.1109/TIE.2017.2674621.
- [25] I. Subotic, D. Gros, Power-balancing dual-port grid-forming power converter control for renewable integration and hybrid AC/DC power systems, *IEEE Transactions on Control of Network Systems* 9 (4) (2022) 1949–1961. doi:10.1109/TCNS.2022.3181551.
- [26] S. K. Kollimalla, M. K. Mishra, N. L. Narasamma, Design and analysis of novel control strategy for battery and supercapacitor storage system, *IEEE Transactions on Sustainable Energy* 5 (4) (2014) 1137–1144. doi:10.1109/TSTE.2014.2336896.
- [27] Thibault Prevost, D3.2 – Overall specifications of the demonstrations, Tech. Rep. D3.2, OSMOSE (2019). URL <https://www.osmose-h2020.eu/wp-content/uploads/2024/10/OSMOSE-D3.2-Overall-specifications-of-the-demonstrations-2019-06-28-v1.pdf>
- [28] H. Gao, T. Jin, C. Feng, C. Li, Q. Chen, C. Kang, Review of virtual power plant operations: Resource coordination and multidimensional interaction, *Applied Energy* 357 (2024) 122284. doi:10.1016/j.apenergy.2023.122284.
- [29] G. Ruan, D. Qiu, S. Sivarajani, A. S. Awad, G. Strbac, Data-driven energy management of virtual power plants: A review, *Advances in Applied Energy* (2024) 00170. doi:10.1016/j.adapen.2024.100170.
- [30] N. Naval, J. M. Yusta, Virtual power plant models and electricity markets—a review, *Renewable and Sustainable Energy Reviews* 149 (2021) 111393. doi:10.1016/j.rser.2021.111393.
- [31] Q. Chen, R. Lyu, H. Guo, X. Su, Real-time operation strategy of virtual power plants with optimal power disaggregation among heterogeneous resources, *Applied Energy* 361 (2024) 122876. doi:10.1016/j.apenergy.2024.122876.
- [32] W. Zhong, J. Chen, M. Liu, M. A. A. Murad, F. Milano, Coordinated control of virtual power plants to improve power system short-term dynamics, *Energies* 14 (4) (2021) 1182. doi:10.3390/en14041182.
- [33] X. Zhu, G. Ruan, H. Geng, Dynamic virtual power plants with frequency regulation capacity, *arXiv preprint arXiv:2406.05976* (2024). doi:10.48550/arXiv.2406.05976.
- [34] V. Haberle, L. Huang, X. He, E. Prieto-Araujo, F. Dorfler, Dynamic ancillary services: From grid codes to transfer function-based converter control, *Electric Power Systems Research* 234 (2024) 110760. doi:10.1016/j.epsr.2024.110760.
- [35] V. Haberle, X. He, L. Huang, E. Prieto-Araujo, F. Dorfler, Optimal dynamic ancillary services provision based on local power grid perception, *IEEE Transactions on Power Systems* (2024) 1–15doi:10.1109/TPWRS.2024.3447410.



- [36] K. De Brabandere, B. Bolsens, J. V. d. Keybus, A. Woyte, J. Driesen, and R. Belmans, "A voltage and frequency droop control method for parallel inverters," *IEEE Trans. Power Electron.*, vol. 22, no. 4, pp. 1107–1115, 2007.
- [37] "Analysis of the synchronisation capabilities of BESS power converters," OSMOSE, European Union Horizon 2020 research and innovation program, Tech. Rep., 2022.
- [38] E. de Espana, "Norma tecnica de supervision de la conformidad de los modulos de generacion de electricidad segun el reglamento ue 2016/631: Tech. rep," 2021.
- [39] J. Shair, X. Xie, W. Liu, X. Li, and H. Li, "Modeling and stability analysis methods for investigating subsynchronous control interaction in largescale wind power systems," *Renewable and Sustainable Energy Reviews*, vol. 135, p. 110420, 2021.
- [40] J. Shair, X. Xie, and G. Yan, "Mitigating subsynchronous control interaction in wind power systems: Existing techniques and open challenges," *Renewable and Sustainable Energy Reviews*, vol. 108, pp. 330–346, 2019.
- [41] D. S. Kirschen and G. Strbac, *Fundamentals of power system economics*. John Wiley & Sons, 2018.
- [42] Fingrid Oyj, *The technical requirements and the prequalification process of fast frequency reserve (FFR)*, Tech. rep., Fingrid Oyj (2023).
- [43] L. Huang, H. Xin, Z. Wang, K. Wu, H. Wang, J. Hu, C. Lu, A virtual synchronous control for voltage-source converters utilizing dynamics of dc-link capacitor to realize self-synchronization, *IEEE Journal of Emerging and Selected Topics in Power Electronics* 5 (4) (2017) 1565–1577. doi:10.1109/JESTPE.2017.2740424.
- [44] L. Kong, C. Wu, J. Xu, J. Wang, Y. Wang, Enhanced DC-link voltage synchronization control for grid-forming photovoltaic systems considering PV power dynamics and grid strength adaptability, *IEEE Transactions on Energy Conversion* (2024) 1–12doi:10.1109/TEC.2024.3460828.
- [45] V. Haberle, L. Huang, X. He, E. Prieto-Araujo, R. S. Smith, and F. Dorfler, "MIMO grid impedance identification of three-phase power systems: Parametric vs. nonparametric approaches," arXiv:2305.00192, 2023.
- [46] L. Ljung, *System Identification: Theory for the User*. Prentice-Hall, New Jersey, 1999.
- [47] T. Soderstrom, *Errors-In-Variables Methods in System Identification*. Springer, Cham, Switzerland, 2018.
- [48] Z. Yang, C. Mei, S. Cheng, and M. Zhan, "Comparison of impedance model and amplitude–phase model for power-electronics-based power system," *IEEE Journal of Emerging and Selected Topics in Power Electronics*, vol. 8, no. 3, pp. 2546–2558, 2019.
- [49] X. Wang, L. Harnefors, and F. Blaabjerg, "Unified impedance model of grid-connected voltage-source converters," *IEEE Trans. Power Electron.*, vol. 33, no. 2, pp. 1775–1787, 2017.
- [50] E. Sanchez-Sanchez, D. Gross, E. Prieto-Araujo, F. Dorfler, and O. Gomis-Bellmunt, "Optimal multivariable mmc energy-based control for dc voltage regulation in hvdc applications," *IEEE Trans. Power Del.*, vol. 35, no. 2, pp. 999–1009, 2019.
- [51] K. Zhou, J. Doyle, and K. Glover, *Robust and Optimal Control*. Prentice-Hall, New Jersey, 1996.
- [52] V. Haberle, M. W. Fisher, E. Prieto-Araujo, and F. Dorfler, "Control design of dynamic virtual power plants: An adaptive divide-and-conquer approach," *IEEE Trans. Power Syst.*, vol. 37, no. 5, pp. 4040–4053, 2021.
- [53] Z. Guo, W. Wu, Matching synchronous machine control for improving active support of grid-forming PV systems with enhanced DC voltage dynamics, *Journal of Modern Power Systems and Clean Energy* (2024) 1–12doi:10.35833/MPCE.2023.000624.
- [54] X. He, M. A. Desai, L. Huang, F. Dorfler, Cross-forming control and fault current limiting for grid-forming inverters, *IEEE Transactions on Power Electronics* 40 (3) (2025) 3980–4007. doi:10.1109/TPEL.2024.3500885.
- [55] P. Kundur, *Power System Stability and Control*. McGraw-Hill, 1994.
- [56] A. Yazdani and R. Iravani, *Voltage-sourced converters in power systems*. Wiley Online Library, 2010, vol. 39.



- [57] A. Tayyebi, D. Gros, A. Anta, F. Kupzog, and F. Dorfler, "Frequency stability of synchronous machines and grid-forming power converters," *IEEE Trans. Emerg. Sel. Topics Power Electron.*, vol. 8, no. 2, pp. 1004–1018, 2020.
- [58] IEEE 13 node test feeder (1992). URL <https://cmte.ieee.org/pes-testfeeders/wp-content/uploads/sites/167/2017/08/feeder13.zip>
- [59] D. P. Bertsekas, *Nonlinear Programming*. Scientific, Athena, Belmont Massachusetts, 1999.
- [60] I. J. Goodfellow, J. Shlens, and C. Szegedy, "Explaining and harnessing adversarial examples," *arXiv:1412.6572*, 2014.
- [61] E. Moulay, V. Lechappe, and F. Plestan, "Properties of the sign gradient descent algorithms," *Information Sciences*, vol. 492, pp. 29–39, 2019.
- [62] M. Riedmiller and H. Braun, "A direct adaptive method for faster backpropagation learning: The rprop algorithm," in *IEEE international conference on neural networks*. IEEE, 1993, pp. 586–591.